SOTTOSTRUTTURE IN AMMASSI DI GALASSIE

COLLISIONI DI AMMASSI

(MERGER)

Collisioni Ammasso - Ammasso di galassie

ottico! Girardi e Biviano 2002
X: Sarazin 96 e 2002
NON TERMICO

es. Rood-Sastry

classificazione morfologica ⟷ formazione / evoluzione degli Ammassi

presenza di sottostrutture

$z = 0$

sì! per un > 50%, sottostrutture = 10% M_{TOT} (Girardi et al 97)

solo un ≲ 10% di Ammassi ha merger importanti (es. 1:1, 3:1)

(3) filamenti delle LLS large scale structure

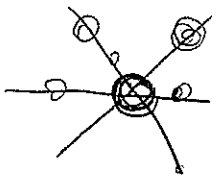

infalli di gruppi

cluster mergers

Dalle cosmologie:

Ω_M alto: evoluzione continua fino ad oggi (densità di materia è alta!)

Ω_M basso: tutto congelato, poca evoluzione con z

pochi merger importanti!
devo andare a $z \sim 1$ per vedere evoluzione importante

(ammassi a filamento di P. Rosati I. Ioio)

quadro osservativo non è chiaro!

Amm. + grossi formati più di recente quindi più sottostrutturati

cD: the cluster is dominated by a central cD galaxy (example: A2199). cD galaxies were defined by Mathews, Morgan, and Schmidt (1964) as galaxies with the nucleus of a very luminous elliptical galaxy embedded in an extended, amorphous optical halo of low surface brightness. They are generally found near the center of dense clusters and groups of galaxies. They are, as a class, the most luminous galaxies known if one excludes nuclear sources, such as quasars. cD galaxies are discussed extensively in Sec. II.J.1.

B: binary—the cluster is dominated by a pair of luminous galaxies [example: A1656 (Coma)].

L: line—at least three of the brightest galaxies appear to be in a straight line [example: A426 (Perseus)].

C: core—four or more of the ten brightest galaxies form a cluster core, with comparable galaxy separations [example: A2065 (Corona Borealis)].

F: flat—the brightest galaxies form a flattened distribution on the sky [example: A2151 (Hercules)].

I: irregular—the distribution of brightest galaxies is irregular, with no obvious center or core (example: A400).

Rood and Sastry (1971) give classifications for low-redshift Abell clusters on this system. They show that these classifications form a bifurcated sequence, which can be represented by a "tuning-fork" diagram [Fig. 3(a)]. This sequence is correlated with the sequence of *regular* to *irregular* clusters in the sense that clusters on the left of the diagram (cD and B) are regular and those to the right (F and I) are irregular. Rich clusters are more or less equally distributed among the three arms of the diagram.

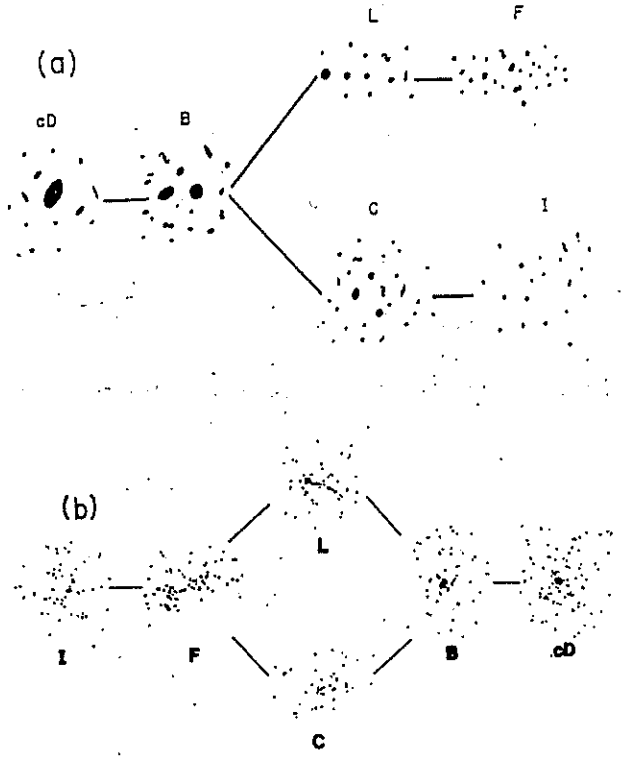

FIG. 3. (a) The Rood-Sastry (1971) cluster classification scheme. (b) The revised Rood-Sastry classes from Struble and Rood (1982).

Recently, Struble and Rood (1982,1984) have proposed a revised version of the RS classification system. The definitions have been revised slightly, and a number of subclasses of the main RS classes have been proposed. More significantly, Struble and Rood have rearranged the "tuning fork" diagram into a "split linear" diagram [Fig. 3(b)], based on systematic trends in the galaxy distribution and content of clusters. This new scheme was devised in part from a comparison to numerical N-body simulations of the collapse of clusters (White, 1976c; Carnevali *et al.*, 1981; Farouki *et al.*, 1983; also see Fig. 4 below). Struble and Rood propose that this sequence represents an evolutionary sequence of clusters from irregular I to cD clusters.

Morgan (1961) and Oemler (1974) have constructed classification systems based on the galactic content of clusters [that is, the fraction of cluster galaxies which are spirals (Sp's), disk galaxies without spiral structure (SO's), or elliptical (E's)]. Morgan (1961) classified clusters as *type i* if they contained large numbers of spirals and as *type ii* if they contained few spirals. Oemler (1974) has refined this system, defining three classes of clusters: *spiral-rich* clusters, in which spirals (Sp) are the most common galaxies; *spiral-poor* clusters, in which spirals are less common and SO's are the most common galaxies; and *cD* clusters, which are dominated by a central cD galaxy and in which the great majority of galaxies are ellipticals or SO's.

These systems of classification are empirically found to be highly correlated, and can roughly be mapped into a one-dimensional sequence running from *regular* clusters to *irregular* clusters (Abell, 1965,1975). As shown in Table II, *regular* clusters are highly symmetric in shape and have a core with a high concentration of galaxies toward the center. Subclustering is weak or absent in *regular* clusters. In contrast, *irregular* clusters have little symmetry or central concentration and often show significant subclustering. This suggests that the *regular* clusters are, in some sense, dynamically relaxed systems, while the *irregular* clusters are dynamically less evolved and have preserved roughly their distribution of formation. Additional evidence that regular clusters are dynamically relaxed is provided in Secs. II.F, II.G, and II.J.1, and the nature of the dynamical processes that might produce this relaxation is discussed in Sec. II.I.

Regular clusters tend to be *compact* (Zwicky type), Bautz-Morgan *type I* to *II*, Rood-Sastry types *cD* or *B*, Morgan *type ii*, Oemler *spiral-poor* or *cD* clusters. These last four correlations indicate a connection between the dynamical state and galactic content of clusters. There is no one-to-one correlation between the morphology of a cluster and its richness; *regular* clusters are always rich, while *irregular* clusters may be either rich or sparse. However, *regular* clusters tend to have higher central galaxy densities than *irregular* clusters, because they are at least as rich and more compact.

predicts that L_1 increases with cluster richness, which is not really observed (Sandage, 1976). However, Schechter and Peebles (1976) have argued that the near constancy of L_1 results from a selection effect (that is, the observed sample is biased), and that the statistical hypothesis may still be valid.

Alternatively, the brightest cluster galaxies may be affected by special physical processes, such as the tidal interactions or mergers of galaxies (Peach, 1969; Ostriker and Tremaine, 1975; Richstone, 1975; Hausman and Ostriker, 1978). Evidence that this may indeed be the case is given in Sec. II.J.1.

While the luminosity functions of many clusters are reasonably well represented by the Schechter or Abell form with a universal value of M^*, significant departures exist in a number of clusters (Oemler, 1974; Mottmann and Abell, 1977; Dressler, 1978b). These departures include variations in the value of M^*, variations in the slope of the faint end of the luminosity function [α in Schechter's form, Eq. (2.3)], and variations in the steepness of the bright end of the luminosity function (Dressler, 1978b). These variations are, in many cases, correlated with cluster morphology (Sec. II.E). The variations in M^* and α probably reflect variations in the conditions in the cluster at its formation, while the variations in the bright end slope may result from evolutionary changes, such as the tidal interaction or merging of massive galaxies (Richstone, 1975; Hausman and Ostriker, 1978). In particular, the clusters with the steepest luminosity functions at the bright end often contain cD galaxies (Dressler, 1978b); this may indicate that the brighter galaxies were either eliminated by mergers to form the cD or diminished in brightness through tidal stripping (Sec. II.J.1).

Turner and Gott (1976a) have shown that the luminosity function of galaxies in small groups is well represented by Eq. (2.3). In fact, Bahcall (1979a) has suggested that the luminosity function of all galaxian systems—from single galaxies (in or out of clusters) to the groups and clusters themselves—can be fit in a single function similar to the Schechter form [Eq. (2.3)].

E. Morphological classification of clusters

A number of different cluster properties have been used to construct morphological classification systems for clusters. Somewhat surprisingly, these different systems are highly correlated, and it appears that clusters can be represented very crudely as a one-dimensional sequence, running from *regular* to *irregular* clusters (Abell, 1965,1975). There is considerable evidence that the regular clusters are dynamically more evolved and relaxed than the irregular clusters. The various morphological classification schemes are described below, and the way in which they fit into the one-dimensional sequence is summarized in Table II, which is adapted from Abell (1975) and Bahcall (1977a).

Zwicky *et al.* (1961—1968) classified clusters as *compact, medium compact,* or *open*. A *compact* cluster has a single pronounced concentration of galaxies, with more than ten galaxies appearing in contact as seen on the plate. A *medium compact* cluster has either a single concentration with ten galaxies separated by roughly their own diameters, or several concentrations. An *open* cluster lacks any pronounced concentration of galaxies.

Bautz and Morgan (1970) give a classification system based on the degree to which the cluster is dominated by its brightest galaxies. Bautz-Morgan *type I* clusters are dominated by a single, central cD galaxy; cD galaxies have the most luminous and extensive optical emission found in galaxies (see Sec. II.J.1). In *type II* clusters, the brightest galaxies are intermediate between cD and normal giant ellipticals, while in *type III*, there are no dominating cluster galaxies. *Type I-II* and *type II-III* are intermediates. Leir and van den Bergh (1977) have classified 1889 rich Abell clusters on the Bautz-Morgan system, and some of the newer southern catalogs (e.g., White and Quintana, 1985) give Bautz-Morgan types for their clusters.

The original Rood-Sastry (1971) classification system is based on the nature and distribution of the ten brightest cluster galaxies. Basically, the six Rood-Sastry (RS) classes are defined as follows:

TABLE II. Properties of morphological classes of clusters.

Property	Regular	Intermediate	Irregular
Zwicky type	compact	medium-compact	open
Bautz-Morgan type	I,I-II,II	II,II-III	II-III,III
Rood-Sastry type	cD,B,L,C	L,C,F	F,I
Galactic Content	elliptical rich	spiral poor	spiral rich
E:SO:Sp	3:4:2	1:4:2	1:2:3
Morgan type	ii	i-ii	i
Oemler type	cD, spiral poor	spiral poor	spiral rich
Symmetry	spherical	intermediate	irregular
Central concentration	high	moderate	low
Subclustering	absent	moderate	significant
Richness	rich	rich-moderate	rich-poor
	$n^* \approx 10^2$	$n^* \gtrsim 10^1$	$n^* \gtrsim 10^0$

Metodi di analisi: ottico x le galassie

1D cf. con gaussiane

2D isocontorni di equidensità nelle distribuzione di pols

(Kernel gaussiani o no metodi wavelet)

3D • correlazioni fra velocità e posizione

• gradienti di velocità

EST CON SIMULAZIONI MONTECARLO

TIPO DI METODO → INFO SU ANGOLO α DI PROIEZIONE

Sottostrutture possono essere

1 sistemi in fase di fusione ($t \gtrsim t_{core-core}$)

2 sistemi entro Ammasso già rilassato dinamicamente (gruppo perde parte esterne x effetti mareali ma core + denso sopravvive!) ($t >> t_{core-core}$)

3 gruppi legati: destinati a fare merger ($t < t_{core-core}$)

4 gruppi slegati, visti in proiezione!

legati-slegati dal criterio di Newton

↳ $T + U \leq 0$ $\quad V_p^2 R_p \leq 2 G M_{TOT} \sin\alpha \cos\alpha$

$R_p = R_\beta \cos\alpha$

$V_p = V_\beta \sin\alpha$

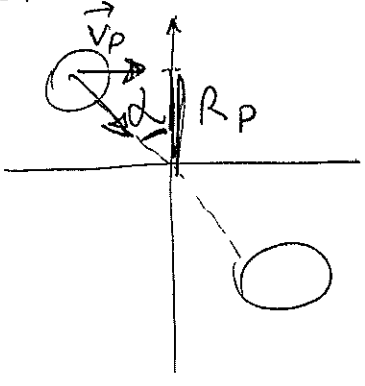

per eventuali approfondimenti
su moodle

Chapter 1

OPTICAL ANALYSIS OF CLUSTER MERGERS

Marisa Girardi
Dipartimento di Astronomia
Università degli Studi di Trieste
girardi@ts.astro.it

Andrea Biviano
Osservatorio Astronomico di Trieste
INAF
biviano@ts.astro.it

Abstract An increasing amount of data has revealed that many clusters are very complex systems. Optical analyses show that several clusters contain subsystems of galaxies, suggesting that they are still in the phase of dynamical relaxation. Indeed, there is a growing evidence that these subsystems arise as the consequence of group/cluster mergers. We here review the state of art of optical search and characterization of cluster substructures. We describe the effects cluster mergers have on optical measures of cluster dynamics, and on the properties of cluster member galaxies. We also discuss cluster mergers in relation to the large scale structure of the universe.

Keywords: Clusters: general, galaxies: evolution, cosmology, interactions

1. INTRODUCTION

Until the 80's clusters have been modeled as virialized spherically symmetric systems (e.g., Kent & Gunn 1982). Rather, clusters often contain subsystems of galaxies, usually called substructures or subclusters. Indeed, in the hierarchical scenario of large scale formation it is quite natural to expect that clusters form from the merger of small subclumps (e.g., Colberg et al. 1999). In this context, the presence of

Modello a 2 corpi (2 punti massa) in centro head-on ($\vec{L}=0$)

può essere risolto analiticamente
(con angolo di sviluppo χ)

$$\ddot{R} = -\frac{M_{TOT}\,G}{R^2}$$ → vedi eq cinet. di Gregory e Thompson 84

→ $M_{TOT} = M_{TOT}(\alpha)$

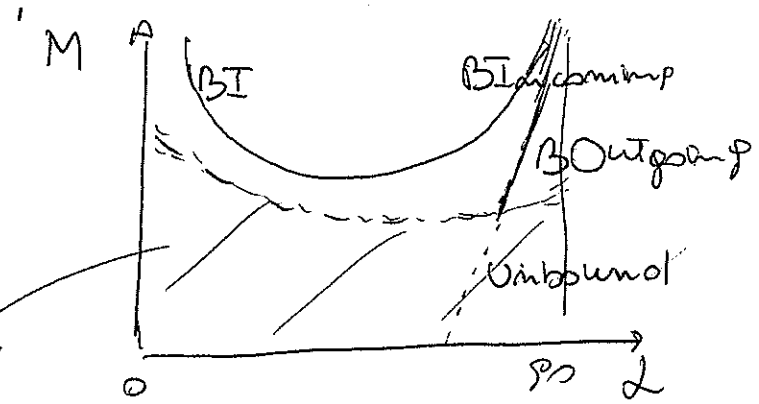

criterio di Newton

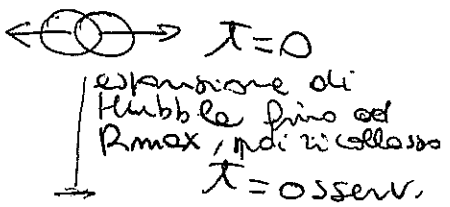

$t=0$ età Universo se si vuole osservare prima delle collisione

STIME DELLA CINEMATICA DEL MERGER SARAZIN2002

oppure

Δt dopo collisione DATO ESTERNO !

DALLA CINEMATICA GAL S.: V_p, D_p, MASS RATIO,
STUDI A GRANDI R MA X HA + STATISTICA
vogliamo α (Tempi da X)

anche da gravitational lensing

DOPO CORE-CORE

OFFSETS

da Ch. ottica-X

NON COLLIS. ← & → COLLISION.

Boschin et al 2010

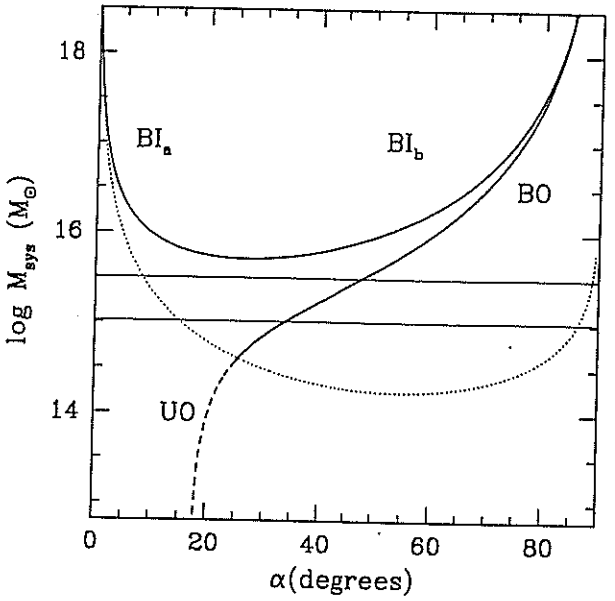

Fig. 10. System mass vs. projection angle for bound and unbound solutions (thick solid and thick dashed curves, respectively) of the two-body model applied to the E and SN+SW subsystems. Labels BI_a and BI_b indicate the bound and incoming, i.e., collapsing solutions (thick solid curve). Label BO indicates the bound outgoing, i.e., expanding solutions (thick solid curve). Label UO indicates the unbound outgoing solutions (thick dashed curve). The horizontal lines give the range of observational values of the mass system with a 50% error. The thin dashed curve separates bound and unbound regions according to the Newtonian criterion (above and below the thin dashed curve, respectively).

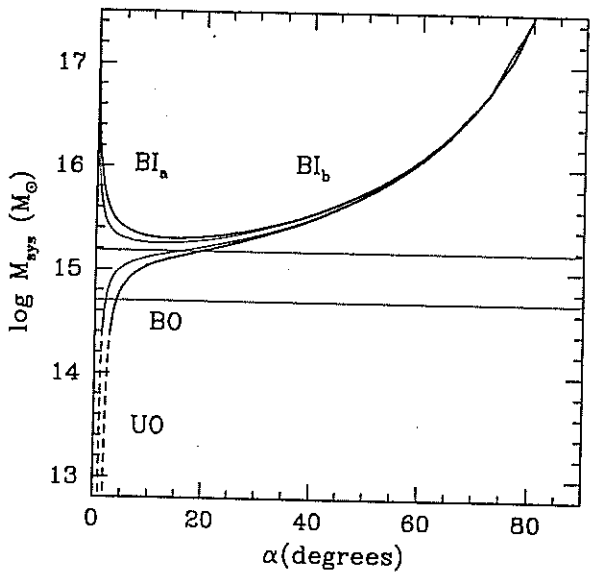

Fig. 11. The same that in Fig. 10 but for the NW and SW subsystems. Thick and thin lines give the results for $V_{rf,LOS} \sim 100$ and 50 km s^{-1}, respectively.

of the shock $\mathcal{M} \sim 2.8$ as inferred by B09 from the radio spectral index of A2345–2. The Mach number is defined to be $\mathcal{M} = v_s/c_s$, where v_s is the velocity of the shock and c_s is the sound speed in the pre-shock gas (see e.g., Sarazin 2002 for a review). The value of c_s, obtained from our estimate of $\sigma_{V,E} \sim 900$ km s^{-1}, leads to a value of $v_s \sim 2.5\times10^3$ km s^{-1}. Assuming the shock velocity to be a constant, the shock covered a $\sim 0.9\ h_{70}^{-1}$ Mpc scale (i.e., the distance of the relic from the cluster center) in a time of ~0.35 Gyr. We assume this time as our estimate of t. Although the velocity of the shock is not constant, studies based on numerical simulations show how the variation in v_s is much smaller than the variation in the relative velocity of the subclumps identified with their dark matter components (see Fig. 4 of Springel & Farrar 2007, and Fig. 14 of Mastropietro & Burkert 2008), thus our rough estimate of t is acceptable as a first order approximation.

The bimodal model solution gives the total system mass M_{sys}, i.e. the sum of the masses of the E+SW+NW groups, as a function of α, where α is the projection angle between the plane of the sky and the line connecting the centers of the two clumps (e.g., Gregory & Thompson 1984). Figure 10 compares the bimodal-model solutions with the observed mass of the system considering a 50% uncertainty band. The present solutions span the bound outgoing solutions (i.e., expanding), BO; the bound incoming solutions (i.e., collapsing), BI_a and BI_b; and the unbound outgoing solutions, UO. For the incoming case, there are two solutions because of the ambiguity in the projection angle α. The BO solution is the only one to be consistent with the observed mass range leading to a $\alpha \sim 40$–50 degrees. The BO solution means that the E group is moving towards East going in the opposite direction with respect to the observer, while the SW+NW complex is moving toward West toward the observer. The angle estimate means that the true spatial distance between the two subclumps is ~1.3–1.5 h_{70}^{-1} Mpc and that the real, i.e. deprojected, velocity difference is $V_{rf} \sim 1000$–1250 km s^{-1}. We note that the present relative velocity between galaxy clumps is smaller than the shock velocity, i.e., the regime is not stationary, but this is expected when comparing shock and collisionless components in numerical simulations (Springel & Farrar 2007; Mastropietro & Burkert 2008). The deprojected velocity difference of the two clumps at the cross core time is $V_{rf} \sim 2000$–2800 km s^{-1}, i.e. comparable to that of the shock as expected.

As for the second collision, the values of relevant parameters for the two-clump system (the SW and the NW groups) are $V_{rf} \sim 0$ km s^{-1} (since we do not see any significant velocity difference), $D \sim 0.3\ h_{70}^{-1}$ Mpc and $M_{sys} \sim 1.1 + 0.5 \sim 1.6\times10^{15}\ h_{70}^{-1}\ M_\odot$. In our scenario this merger is more recent than the above one and thus we assume a time $t \sim 0.2$ Gyr.

Figure 11 shows the results for $V_{rf} = 50$ km s^{-1} and $V_{rf} = 100$ km s^{-1}. The BO solution is well acceptable with $\alpha \sim 2$–20°. This means that the SW group is moving toward South and the NW group towards North and, as someway expected from the observations, the NW and SW groups define a direction almost parallel to the plane of the sky. The true spatial distance is similar to the projected one. The real velocity difference has a huge uncertainty due to its dependence from the very uncertain α value. Notice that this merger should be considered of minor importance with respect to the main one described above, thus here the bimodal model is likely a worse representation of the reality than the above case.

In conclusion, we recover from our toy model quantitative results consistent with the global scenario. Thus, our analysis of the internal cluster dynamics well supports the "outgoing merger shocks" model proposed by B09. We also present an explanation for the relics asymmetry and the peculiarity of A2345–1. Our explanation is based on the internal structure of A2345, rather than on a possible merger with an external, close group (e.g. the group "X1" detected by B09). Before applying more reliable approaches to the study of A2345 internal dynamics, an improvement of the present observational picture would be very useful,

Sarazin 2002

Chapter 1

THE PHYSICS OF CLUSTER MERGERS

Craig L. Sarazin
Department of Astronomy
University of Virginia
P. O. Box 3818
Charlottesville, VA 22903-0818, USA
sarazin@virginia.edu

Abstract Clusters of galaxies generally form by the gravitational merger of sma clusters and groups. Major cluster mergers are the most energetic eve in the Universe since the Big Bang. Some of the basic physical prop ties of mergers will be discussed, with an emphasis on simple analy arguments rather than numerical simulations. Semi-analytic estima of merger rates are reviewed, and a simple treatment of the kinema of binary mergers is given. Mergers drive shocks into the intraclus medium, and these shocks heat the gas and should also accelerate n thermal relativistic particles. X-ray observations of shocks can be u to determine the geometry and kinematics of the merger. Many cl ters contain cooling flow cores; the hydrodynamical interactions of th cores with the hotter, less dense gas during mergers are discussed. A result of particle acceleration in shocks, clusters of galaxies should c tain very large populations of relativistic electrons and ions. Electr with Lorentz factors $\gamma \sim 300$ (energies $E = \gamma m_e c^2 \sim 150$ MeV) expected to be particularly common. Observations and models for radio, extreme ultraviolet, hard X-ray, and gamma-ray emission fr nonthermal particles accelerated in these mergers are described.

Introduction

Major cluster mergers are the most energetic events in the Unive since the Big Bang. Cluster mergers are the mechanism by which cl ters are assembled. In these mergers, the subclusters collide at velocit of ~2000 km/s, releasing gravitational binding energies of as much $\gtrsim 10^{64}$ ergs. During mergers, shocks are driven into the intraclus medium. In major mergers, these hydrodynamical shocks dissipate e

ergies of $\sim 3 \times 10^{63}$ ergs; such shocks are the major heating source for the X-ray emitting intracluster medium. The shock velocities in merger shocks are similar to those in supernova remnants in our Galaxy, and we expect them to produce similar effects. Mergers shocks should heat and compress the X-ray emitting intracluster gas, and increase its entropy. We also expect that particle acceleration by these shocks will produce relativistic electrons and ions, and these can produce synchrotron radio, inverse Compton (IC) extreme ultraviolet (EUV) and hard X-ray, and gamma-ray emission.

In this chapter, I will review some of the basic physics of cluster mergers. As later chapters discuss the optical, X-ray, and radio observations of mergers, I will concentrate of theoretical issues. Also, because later chapters discuss simulations of cluster mergers and of large scale structure, I will mainly discuss analytical or semi-analytical aspects of cluster mergers. In § 1.1, semi-analytic estimates of merger rates based on Press-Schechter theory are reviewed. Some simple estimates of the kinematics of binary cluster mergers are given in § 1.2. The thermal effects of merger shocks are discussed in § 2, with an emphasis on determining the physical conditions in mergers from X-ray observations of temperatures and densities. Many clusters and groups contain cooling flow cores. During a merger, these cool cores will interact hydrodynamically with the hotter, more diffuse intracluster gas (§ 3). This can lead to the disruption of the cooling flow core, as discussed in § 3.1. Recently, the Chandra X-ray Observatory has detected a number of "cold fronts" in merging clusters, which apparently are cool cores moving through hot, shock heated, diffuse cluster gas (§ 3.2). Relativistic particles may be accelerated or reaccelerated in merger shocks or turbulence generated by mergers. The nonthermal effects of mergers are discussed in § 4. The resulting radio, extreme ultraviolet, hard X-ray, and gamma-ray emission is described.

1. BASIC MERGER RATES AND KINEMATICS

1.1. ESTIMATES OF MERGER RATES

The rates of cluster mergers as a function of the cluster masses and redshift can be estimated using a simple formalism originally proposed by Press & Schechter (1974, hereafter PS), and developed in more detail by Bond et al. (1991) and Lacey & Cole (1993), among others. Comparisons to observations of clusters and to numerical simulations show that PS provides a good representation of the statistical properties of clusters, if the PS parameters are carefully selected (e.g., Lacey & Cole 1993; Bryan & Norman 1998). This formalism assumes that galaxies and clusters grow by the gravitational instability of initially small amplitude gaussian density fluctuations generated by some process in the early Universe. The fluctuation spectrum is assumed to have larger amplitudes on smaller scales. Thus, galaxies and clusters form hierarchically, with lower mass objects (galaxies and groups of galaxies) forming before larger clusters. These smaller objects then merge to form clusters.

In the extended PS formalism, the density fluctuations in the Universe are smoothed on a variety of mass scales. Regions are assumed to collapse when their density exceeds a critical value, which is usually taken to be the density for the collapse for an isolated, spherical mass concentration of the same mass. If one smooths the density fluctuations in some region on a variety of mass scales, the average density may exceed the critical density for collapse on a variety of different mass scales. The assumption of the extended PS formalism is that material is associated with the largest mass scale for which collapse has occurred, and that smaller mass scales have merged into the larger object. With these assumptions, the PS formalism allows one to estimate the abundance of clusters as a function of their mass, and the rates at which clusters merge.

Let $n(M,z)dM$ be the comoving number density of clusters with masses in the range M to $M + dM$ in the Universe at a redshift of z. According to PS, the differential number density is given by

$$n(M,z)\,dM = \sqrt{\frac{2}{\pi}}\,\frac{\overline{\rho}}{M^2}\,\frac{\delta_c(z)}{\sigma(M)}\left|\frac{d\,\ln\,\sigma(M)}{d\,\ln\,M}\right|\,\exp\left[-\frac{\delta_c^2(z)}{2\sigma^2(M)}\right]\,dM\,, \quad (1)$$

where $\overline{\rho}$ is the current mean density of the Universe, $\sigma(M)$ is the current rms density fluctuation within a sphere of mean mass M, and $\delta_c(z)$ is the critical linear overdensity for a region to collapse at a redshift z.

In Cold Dark Matter models, the initial spectrum of fluctuations can be calculated for various cosmologies (Bardeen et al. 1986). Over the range of scales covered by clusters, it is generally sufficient to consider a power-law spectrum of density perturbations, which is consistent with these CDM models:

$$\sigma(M) = \sigma_8\,\left(\frac{M}{M_8}\right)^{-\alpha}\,, \quad (2)$$

where σ_8 is the present day rms density fluctuation on a scale of 8 h^{-1} Mpc, $M_8 = (4\pi/3)(8\,h^{-1}\,\mathrm{Mpc})^3\bar{\rho}$ is the mass contained in a sphere of radius 8 h^{-1} Mpc, and the scaling with the Hubble constant is $h = H_0/100$. When the scaling with the Hubble constant is not given explicitly, we assume $H_0 = 50$ km s^{-1} Mpc^{-1}, i.e. $h = 0.5$. The exponent α is given

by $\alpha = (n+3)/6$, where the power spectrum of fluctuations varies with wavenumber k as k^n. The observations are generally reproduced with values of $-2 \lesssim n \lesssim -1$, leading to $1/6 \lesssim \alpha \lesssim 1/3$. The normalization of the power spectrum and overall present-day abundance of clusters is set by σ_8. The observed present-day abundance of clusters leads to $\sigma_8 \approx 0.6\Omega_m^{-1/2}$, where $\Omega_m \equiv \bar{\rho}/\rho_c$ is the ratio of the current mass density to the critical mass density, $\rho_c = 3H_0^2/(8\pi G)$ (e.g., Bahcall & Fan 1998).

The evolution of the density of clusters is encapsulated in the critical over-density $\delta_c(z)$ in equation (1). In general, $\delta_c(z) \propto 1/D(t)$, where $D(t)$ is the growth factor of linear perturbations as a function of cosmic time t (see Peebles 1980, § 11 for details). Expressions for the $\delta_c(z)$ in different cosmological models are:

$$\delta_c(z) = \begin{cases} \frac{3}{2} D(t_0) \left[1 + \left(\frac{t_\Omega}{t}\right)^{\frac{2}{3}}\right] & (\Omega_m < 1\,,\ \Omega_\Lambda = 0) \\ \frac{3(12\pi)^{\frac{2}{3}}}{20} \left(\frac{t_\Omega}{t}\right)^{\frac{2}{3}} & (\Omega_m = 1\,,\ \Omega_\Lambda = 0) \\ \frac{D(t_0)}{D(t)} \left(\frac{3(12\pi)^{\frac{2}{3}}}{20}\right) (1 + 0.0123\ \log \Omega_z) & (\Omega_m + \Omega_\Lambda = 1) \end{cases} \tag{3}$$

Here, Ω_Λ gives the contribution due to a cosmological constant Λ, where $\Omega_\Lambda \equiv \Lambda/(3H_0^2)$. For the open model ($\Omega_m < 1$, $\Omega_\Lambda = 0$), $t_\Omega \equiv \pi H_0^{-1} \Omega_m (1 - \Omega_m)^{-\frac{3}{2}}$ represents the epoch at which a nearly constant expansion takes over and no new clustering can occur. The growth factor can be expressed as

$$D(t) = \frac{3\ \sinh\eta\,(\sinh\eta - \eta)}{(\cosh\eta - 1)^2} - 2 \tag{4}$$

where η is the standard parameter in the cosmic expansion equations (Peebles 1980, eqn. 13.10)

$$\begin{aligned} \tfrac{1}{1+z} &= \tfrac{\Omega_m}{2(1-\Omega_m)} (\cosh\eta - 1)\ , \\ H_0 t &= \tfrac{\Omega_m}{2(1-\Omega_m)^{\frac{3}{2}}} (\sinh\eta - \eta)\ . \end{aligned} \tag{5}$$

The solution for δ_c in the Einstein-de Sitter model ($\Omega_m = 1$, $\Omega_\Lambda = 0$) can be obtained from the open model solution by the limit $t_\Omega/t \to \infty$. The expression for δ_c in the flat model ($\Omega_m + \Omega_\Lambda = 1$) is an approximation given by Kitayama & Suto (1996). Here Ω_z is the value of the mass density ratio Ω_m at the redshift z,

$$\Omega_z = \frac{\Omega_m (1+z)^3}{\Omega_m (1+z)^3 + \Omega_\Lambda}\ . \tag{6}$$

In this model the growth factor can be written as

$$D(x) = \frac{(x^3+2)^{1/2}}{x^{3/2}} \int_0^x x^{3/2} (x^3+2)^{-3/2} dx \tag{7}$$

(Peebles 1980, eqn. 13.6) where $x_0 \equiv (2\Omega_\Lambda/\Omega_m)^{1/3}$ and $x = x_0/(1+z)$

The PS formalism also provides estimates of the merger history, rates and probabilities for clusters. For example, the probability that a cluste with a mass M_0 at the present time t_0 had a progenitor with a mass o M at an earlier time $t < t_0$ is given by

$$\frac{dp}{dM}(M, t|M_0, t_0) = \frac{\delta_c(t) - \delta_c(t_0)}{\sqrt{2\pi}\,[\sigma^2(M) - \sigma^2(M_0)]^{3/2}} \left(\frac{M_0}{M}\right) \left|\frac{d\,\sigma^2(M)}{d\,M}\right| \exp\left\{-\frac{[\delta_c(t) - \delta_c(t_0)]^2}{2\,[\sigma^2(M) - \sigma^2(M_0)]}\right\}\ . \tag{8}$$

Similarly, the probability that a cluster of mass M undergoes a merge with cluster of mass ΔM per unit time is given by

$$\frac{d^2p}{d\Delta M\,dt} = \sqrt{\frac{2}{\pi}} \frac{\delta_c(z)}{\sigma(M')} \left|\frac{d\,\ln\delta_c(z)}{dt}\right| \left|\frac{d\,\ln\sigma(M')}{d\,M'}\right| \left[1 - \frac{\sigma^2(M')}{\sigma^2(M)}\right]^{-3/2} \times \exp\left\{-\frac{\delta_c^2(z)}{2} \left[\frac{1}{\sigma^2(M')} - \frac{1}{\sigma^2(M)}\right]\right\}\ , \tag{9}$$

where $M' = M + \Delta M$.

These probability distributions can be used to make Monte Carl simulations of the merger histories which produced clusters of a variou masses at present. Figure 1.1 shows one such "merger tree" for a cluste with a mass of $10^{15} h^{-1}\,M_\odot$ at the present time (Randall et al. 2001). A least to the extent that the development of a cluster can be treated a a series of separate, discrete merger events separated by periods of ap proximate equilibrium (the "punctuated equilibrium" model; Cavalier et al. 1999), these merger histories can be used to determine the effect of mergers on clusters.

1.2. ESTIMATES OF MERGER KINEMATIC

I now give some simple analytic arguments to estimate the kinematic of an individual binary merger collision. The kinematic quantities de scribing the merger are defined in Figure 1.2, which is taken from Ricke & Sarazin (2001). The two subclusters have masses M_1 and M_2. Le d be the separation of the centers of the two subclusters, let v be th relative velocity of the centers, and let b be the impact parameter of th collision.

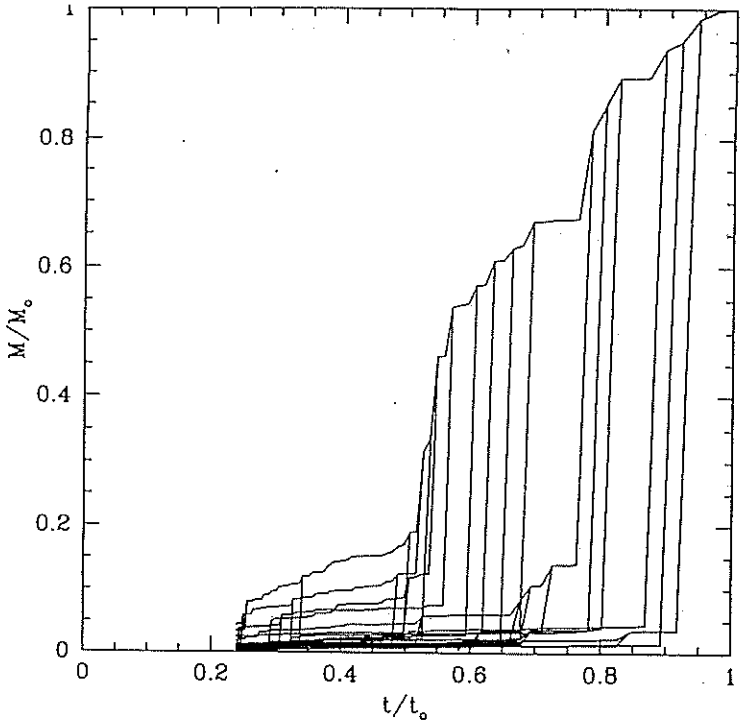

Figure 1.1. An example of a PS merger tree for a cluster of galaxies with a final mass of $M_0 = 10^{15} h^{-1}\, M_\odot$ (Randall et al. 2001). The mass is shown as a function of the age of the Universe t; the present age is t_0. This model was for an open Universe with $\Omega_m = 0.3$ and $\Omega_\Lambda = 0$.

1.2.1 Turn-Around Distances.

Assume that the two subclusters of mass M_1 and M_2 merge at some time $t_{\rm merge}$ (the age of the Universe at the time of the merger). It is assumed that the two subclusters have fallen together from a large distance d_0 with (possibly) nonzero angular momentum. (The exact value of d_0 does not affect the collision velocity very strongly as long as it is large and the infall velocity approaches free-fall from infinity.) For the purpose of computing the initial relative velocity, we approximate the two clusters as point masses. We assume that the two subclusters were initially expanding away from one another in the Hubble flow, and that their radial velocity was zero at their greatest separation d_0. If we assume that the two subclusters dominate the mass in the region of the Universe they occupy, we can treat their initial expansion and recollapse as the orbit of two point masses, and Kepler's Third Law gives the greatest separation as

$$d_0 \approx [2G(M_1+M_2)]^{1/3} \left(\frac{t_{\rm merge}}{\pi}\right)^{2/3}$$

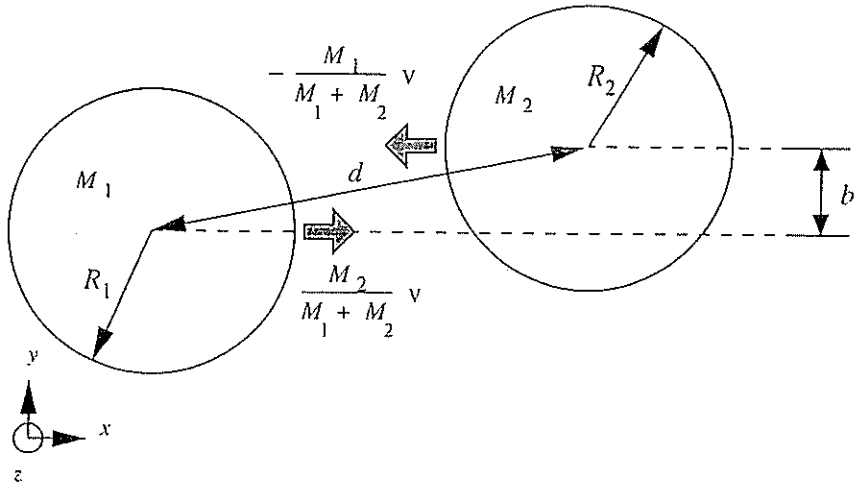

Figure 1.2. A schematic diagram of the kinematics for a merger between two subclusters of masses M_1 and M_2 and radii R_1 and R_2. The separation of the cluster centers is d, and the impact parameter is b, and the initial relative velocity is v.

$$\approx 4.5 \left(\frac{M_1+M_2}{10^{15}\, M_\odot}\right)^{1/3} \left(\frac{t_{\rm merge}}{10^{10}\ {\rm yr}}\right)^{2/3} {\rm Mpc}\,. \qquad (10)$$

1.2.2 Merger Velocities.

At the separation d_0, the clusters are assumed to have zero relative radial velocity; hence their orbital angular momentum and energy are

$$\begin{aligned} J_{\rm orb} &\approx m v_0 d_0 \\ E_{\rm orb} &\approx \frac{1}{2} m v_0^2 - \frac{G M_1 M_2}{d_0}\,, \end{aligned} \qquad (11)$$

where their reduced mass is

$$m \equiv \frac{M_1 M_2}{M_1+M_2}\,, \qquad (12)$$

and v_0 is their initial relative transverse velocity. At the separation d, the relative velocity v is perpendicular to the direction of b, so we can write

$$\begin{aligned} J_{\rm orb} &\approx m v b \\ E_{\rm orb} &\approx \frac{1}{2} m v^2 - \frac{G M_1 M_2}{d}\,. \end{aligned} \qquad (13)$$

Conserving angular momentum and energy, we eliminate v_0 and find

$$v^2 \approx 2G\,(M_1+M_2)\left(\frac{1}{d}-\frac{1}{d_0}\right)\left[1-\left(\frac{b}{d_0}\right)^2\right]^{-1}\,, \qquad (14)$$

or

$$v \approx 2930\left(\frac{M_1+M_2}{10^{15}\,M_\odot}\right)^{1/2}\left(\frac{d}{1\,\mathrm{Mpc}}\right)^{-1/2}\left[\frac{1-\frac{d}{d_0}}{1-\left(\frac{b}{d_0}\right)^2}\right]^{1/2}\,\mathrm{km\,s^{-1}}\,. \qquad (15)$$

1.2.3 Angular Momenta, Impact Parameters, and Transverse Velocities. The remaining kinematic parameter for the merger is the impact parameter b, or equivalently the orbital angular momentum $J_{\rm orb}$ or the initial tangential velocity v_0. In principal, a range of values are possible for mergers of subclusters with similar masses and similar merger epochs $t_{\rm merge}$. The angular momentum will be determined by tidal torques from surrounding material. Thus, I give an estimate of the range of possible values based on the linear-theory result for the dimensionless spin of dark-matter halos; this argument is given in Ricker & Sarazin (2001). The spin parameter λ is defined as (Peebles 1969)

$$\lambda \equiv \frac{J|E|^{1/2}}{GM^{5/2}}\,. \qquad (16)$$

Here J is the total angular momentum of the halo, E is its total energy, and M is its mass. In linear theory, the average value of λ is expected to be approximately constant, independent of the mass of the halo. Recently, Sugerman et al. (2000) have performed a detailed comparison of linear-theory predictions to actual angular momenta of galaxies formed in cosmological N-body/hydro calculations. These simulations did not include cooling or star formation, so at the upper end of the mass range they studied their results should carry over to clusters. They find, in agreement with White (1984), that linear theory overpredicts the final angular momentum of galaxies by roughly a factor of three, with a large ($\sim 50\%$) dispersion in the ratio of the linear-theory prediction to the actual value. However, given the uncertainties, the angular momenta agree with the results in equation (16) for a value of $\lambda \approx 0.05$. Thus, we will assume that the average total angular momenta of clusters of galaxies are given by

$$J \approx \frac{\lambda G M^{5/2}}{|E|^{1/2}}\,, \qquad (17)$$

with $\lambda \approx 0.05$. The normal virial relations for clusters imply that the energies of clusters scale with their mass as $|E| \propto M^{5/3}$, which implies that the angular momenta scale as $J \propto M^{5/3}$ as well.

Let us take the halo to be the final merged cluster. Its final total angular momentum is the sum of the angular momenta of the two subclusters plus the orbital angular momentum $J_{\rm orb}$. Applying equation (17) to the initial masses M_1 and M_2 and the final mass M_1+M_2 and taking the difference gives the orbital angular momentum $J_{\rm orb}$. We assume that the angular momenta are correlated (i.e., that they lie along the same direction), since they are all produced by approximately the same local tidal field. The final energy of the merged cluster is the sum of the energies of the initial subclusters plus the orbital energy $E_{\rm orb}$. The rotational kinetic energies can be ignored as they are only a fraction $\sim 2\lambda^2 \lesssim 1\%$ of the total energies.

Using these relations, the average orbital angular momentum of the merger is found to be

$$J_{\rm orb} \approx \frac{\lambda G M_1 M_2}{\left[\frac{G(M_1+M_2)}{d_0}-\frac{1}{2}v_0^2\right]^{1/2}}\,f(M_1,M_2)\,. \qquad (18)$$

Here, the function $f(M_1,M_2)$ corrects for the internal angular momenta and energy of the subclusters. This correction can be written as

$$f(M_1,M_2) \equiv \frac{(M_1+M_2)^3}{M_1^{3/2}M_2^{3/2}}\left[1-\frac{\left(M_1^{5/3}+M_2^{5/3}\right)}{(M_1+M_2)^{5/3}}\right]^{3/2}\,, \qquad (19)$$

but it only depends on the ratio $(M_</M_>)$ of the smaller to larger mass of the two subclusters. It varies between $4(2^{2/3}-1)^{3/2} \approx 1.80 \le f(M_1,M_2) \le (5/3)^{3/2} \approx 2.15$, so that $f(M_1,M_2) \approx 2$. The kinetic energy term $v_0^2/2$ in the denominator of equation (18) can be shown to be approximately $2\lambda^2 \approx 1\%$ of the potential energy term. Thus, this term can be dropped to yield

$$J_{\rm orb} \approx \lambda M_1 M_2 \sqrt{\frac{G d_0}{M_1+M_2}}\,f(M_1,M_2)\,. \qquad (20)$$

The corresponding initial transverse velocity is

$$\begin{aligned} v_0 &\approx \lambda\sqrt{\frac{G(M_1+M_2)}{d_0}}\,f(M_1,M_2) \\ &\approx 93\left(\frac{\lambda}{0.05}\right)\left(\frac{M_1+M_2}{10^{15}\,M_\odot}\right)^{1/2}\left(\frac{d_0}{5\,\mathrm{Mpc}}\right)^{-1/2}\left(\frac{f}{2}\right)\,\mathrm{km\,s^{-1}}\,. \end{aligned} \qquad (21)$$

Sarazin 2002
su ADS

Chapter 1

THE PHYSICS OF CLUSTER MERGERS

Craig L. Sarazin
Department of Astronomy
University of Virginia
P. O. Box 3818
Charlottesvile, VA 22903-0818, USA
sarazin@virginia.edu

Abstract Clusters of galaxies generally form by the gravitational merger of smaller clusters and groups. Major cluster mergers are the most energetic events in the Universe since the Big Bang. Some of the basic physical properties of mergers will be discussed, with an emphasis on simple analytic arguments rather than numerical simulations. Semi-analytic estimates of merger rates are reviewed, and a simple treatment of the kinematics of binary mergers is given. Mergers drive shocks into the intracluster medium, and these shocks heat the gas and should also accelerate nonthermal relativistic particles. X-ray observations of shocks can be used to determine the geometry and kinematics of the merger. Many clusters contain cooling flow cores; the hydrodynamical interactions of these cores with the hotter, less dense gas during mergers are discussed. As a result of particle acceleration in shocks, clusters of galaxies should contain very large populations of relativistic electrons and ions. Electrons with Lorentz factors $\gamma \sim 300$ (energies $E = \gamma m_e c^2 \sim 150$ MeV) are expected to be particularly common. Observations and models for the radio, extreme ultraviolet, hard X-ray, and gamma-ray emission from nonthermal particles accelerated in these mergers are described.

Introduction

Major cluster mergers are the most energetic events in the Universe since the Big Bang. Cluster mergers are the mechanism by which clusters are assembled. In these mergers, the subclusters collide at velocities of $\sim$2000 km/s, releasing gravitational binding energies of as much as $\gtrsim 10^{64}$ ergs. During mergers, shocks are driven into the intracluster medium. In major mergers, these hydrodynamical shocks dissipate en-

After the clusters have fallen towards one another to a separation d, the impact parameter for the collision is (Figure 1.2)

$$b \approx \left(\frac{v_0}{v}\right) d_0 \,, \qquad (22)$$

where the infall velocity is given by equation (15). Note that equation (22) implies that $b \ll d_o$, so that one can drop the (b/d_0) term in equation (15). Substituting equations (15) & (21) into equation (22) gives

$$\begin{aligned} b &\approx \lambda \sqrt{\tfrac{d_0 d}{2}} \left(1 - \tfrac{d}{d_0}\right)^{-1/2} f(M_1, M_2) \\ &\approx 160 \left(\tfrac{\lambda}{0.05}\right) \left(\tfrac{d}{1\,\mathrm{Mpc}}\right)^{1/2} \left(\tfrac{d_0}{5\,\mathrm{Mpc}}\right)^{1/2} \left(1 - \tfrac{d}{d_0}\right)^{-1/2} \left(\tfrac{f}{2}\right) \mathrm{kpc}\,. \end{aligned} \qquad (23)$$

Thus, most mergers are expected to involve fairly small impact parameters, comparable to the sizes of the gas cores in clusters. Many examples are known of mergers where the X-ray morphology suggests a small offset; an example is the merger in the cluster surrounding Cygnus-A (Markevitch et al. 1999). However, the preceding arguments are approximate and statistical, and mergers with larger impact parameters are also expected to occur; based on the X-ray image and temperature map, it is likely that Abell 3395 is an example of such a merger (Markevitch et al. 1998). Larger impact parameters may occur in mergers involving more than two subclusters. On the other hand, the distribution of impact parameters may be biased to lower values if most mergers occur along large scale structure filaments (e.g., Evrard & Gioia, this volume).

2. THERMAL PHYSICS OF MERGER SHOCKS

The intracluster medium (ICM) is generally close to hydrostatic equilibrium in clusters which are not undergoing strong mergers. The virial theorem then implies that the square of the thermal velocity (sound speed) of the ICM is comparable to the gravitational potential. During a merger, the infall velocities of the subclusters (equation 15) are comparable to the escape velocity, which implies that the square of the infall velocity is larger (by roughly a factor of two) than the gravitational potential. Thus, the motions in cluster mergers are expected to be supersonic, but only moderately so. As a result, one expects that cluster mergers will drive shock waves into the intracluster gas of the two subclusters. Let v_s be the velocity of such a shock wave relative to the preshock intracluster gas. The sound speed in the preshock gas is $c_s = \sqrt{(5/3)P/\rho}$, where P is the gas pressure and ρ is the density. Then,

the Mach number of the shock is $\mathcal{M} \equiv v_s/c_s$. Based on the simple argument given above and confirmed by merger simulations (Schindler & Müller 1993; Roettiger et al. 1999; Ricker & Sarazin 2001; Schindler, this volume), one expects shocks with Mach numbers of $\mathcal{M} \lesssim 3$. Stronger shocks may occur under some circumstances, such as in the outer parts of clusters, or in low mass subclusters merging with more massive clusters. However, in the latter case, the shocks in the less massive subcluster may also be weak if the intergalactic gas in the smaller subcluster is denser than that in the more massive subclusters (§ 3).

Shocks are irreversible changes to the gas in clusters, and thus increase the entropy S in the gas. A useful quantity to consider is the specific entropy per particle in the gas, $s \equiv S/N$, where N is the total number of particles. To within additive constants, the specific entropy of an ideal gas is

$$\begin{aligned} s &= \frac{3}{2} k \ln\left(\frac{P}{\rho^{5/3}}\right) , \\ &= \frac{3}{2} k \ln\left(\frac{T}{\rho^{2/3}}\right) , \end{aligned} \qquad (24)$$

where T is the gas temperature. Observations of X-ray spectra can be used to determine T, while the X-ray surface brightness depends on ρ^2. Thus, one can use X-ray observations to determine the specific entropy in the gas just before and just after apparent merger shocks seen in the X-ray images. Since merger shocks should produce compression, heating, pressure increases, and entropy increases, the corresponding increase in all of these quantities (particularly the entropy) can be used to check that discontinuities are really shocks (e.g., not "cold fronts" or other contact discontinuities, § 3.2).

Markevitch et al. (1999) applied this test to ASCA temperature maps and ROSAT images of Cygnus-A and Abell 3667, two clusters which appeared to show strong merger shocks. (Recent Chandra images have cast doubt on the interpretation of Abell 3667, Vikhlinin et al. 2001b.) In Cygnus-A, the increase in specific entropy in the shocked regions is roughly $\Delta s \approx (3/2)k$. The specific heat per particle q which must be dissipated to produce this change in entropy is $q \approx T\Delta s \approx (3/2)kT$, or about the present specific heat content in the shocked gas. Thus, these observations provide a direct confirmation that merger shocks contribute significantly to the heating of the intracluster gas.

2.1. SHOCK KINEMATICS

The variation in the hydrodynamical variables in the intracluster medium across a merger shock are determined by the standard Rankine–

Hugoniot jump conditions (e.g., Landau & Lifshitz 1959, § 85), if one assumes that all of the dissipated shock energy is thermalized. Consider a small element of the surface of a shock (much smaller than the radius of curvature of the shock, for example). The tangential component of the velocity is continuous at the shock, so it is useful to go to a frame which is moving with that element of the shock surface, and which has a tangential velocity which is equal to that of the gas on either side of the shock. In this frame, the element of the shock surface is stationary, and the gas has no tangential motion. Let the subscripts 1 and 2 denote the preshock and postshock gas; thus, $v_1 = v_s$ is the longitudinal velocity of material into the shock (or alternative, the speed with which the shock is advancing into the preshock gas). Conservation of mass, momentum, and energy then implies the following jump conditions

$$\begin{aligned} \rho_1 v_1 &= \rho_2 v_2 \,, \\ P_1 + \rho_1 v_1^2 &= P_2 + \rho_2 v_2^2 \,, \\ w_1 + \frac{1}{2} v_1^2 &= w_2 + \frac{1}{2} v_2^2 \,. \end{aligned} \tag{25}$$

Here, $w = P/\rho + \epsilon$ is the enthalpy per unit mass in the gas, and ϵ is the internal energy per unit mass. If the gas behaves as a perfect fluid on each side of the shock, the internal energy per unit mass is given by

$$\epsilon = \frac{1}{\gamma_{\rm ad} - 1} \frac{P}{\rho} \,, \tag{26}$$

where $\gamma_{\rm ad}$ is the ratio of specific heats (the adiabatic index) and is $\gamma_{\rm ad} = 5/3$ for fully ionized plasma. The jump conditions can be rewritten as:

$$\begin{aligned} \frac{P_2}{P_1} &= \frac{2\gamma_{\rm ad}}{\gamma_{\rm ad}+1} \mathcal{M}^2 - \frac{\gamma_{\rm ad}-1}{\gamma_{\rm ad}+1} \\ \frac{v_2}{v_1} = \frac{\rho_1}{\rho_2} \equiv \frac{1}{C} &= \frac{2}{(\gamma_{\rm ad}+1)\mathcal{M}^2} + \frac{\gamma_{\rm ad}-1}{\gamma_{\rm ad}+1} \end{aligned} \tag{27}$$

where $C \equiv \rho_2/\rho_1$ is the shock compression.

If one knew the velocity structure of the gas in a merging cluster, one could use these jump condition to derive the temperature, pressure, and density jumps in the gas. At present, the best X-ray spectra for extended regions in clusters of galaxies have come from CCD detectors on ASCA, Chandra, and XMM/Newton. CCDs have a spectral resolution of >100 eV at the Fe K line at 7 keV, which translates into a velocity resolution of >4000 km/s. Thus, this resolution is (at best) marginally insufficient to measure merger gas velocities in clusters. In a few cases with very bright regions and simple geometries, the grating spectrometers on Chandra and especially XMM/Newton may be useful. However, it is likely that the direct determinations of gas velocities in most clusters will wait for the launch of higher spectral resolution nondispersive spectrometers on Astro-E2 and Constellation-X.

At present, X-ray observations can be used to directly measure the temperature and density jumps in merger shocks. Thus, one needs to invert the jump relations to give the merger shock velocities for a given shock temperature, pressure, and/or density increase. If the temperatures on either side of the merger shock can be measured from X-ray spectra, the shock velocity can be inferred from (Markevitch et al. 1999)

$$\Delta v_s = \left[\frac{kT_1}{\mu m_p} (C-1) \left(\frac{T_2}{T_1} - \frac{1}{C} \right) \right]^{1/2} \,, \tag{28}$$

where $\Delta v_s = v_1 - v_2 = [(C-1)/C] v_s$ is the velocity change across the shock, and μ is the mean mass per particle in units of the proton mass m_p. The shock compression C can be derived from the temperatures as

$$\frac{1}{C} = \left[\frac{1}{4} \left(\frac{\gamma_{\rm ad}+1}{\gamma_{\rm ad}-1} \right)^2 \left(\frac{T_2}{T_1} - 1 \right)^2 + \frac{T_2}{T_1} \right]^{1/2} - \frac{1}{2} \frac{\gamma_{\rm ad}+1}{\gamma_{\rm ad}-1} \left(\frac{T_2}{T_1} - 1 \right) \,. \tag{29}$$

Alternatively, the shock compression can be measured directly from the X-ray image. However, it is difficult to use measurements of the shock compression alone to determine the shock velocity, for two reasons. First, a temperature is needed to set the overall scale of the velocities; as is obvious from equation (27), the shock compression allows one to determine the Mach number $\mathcal{M}$ but not the shock velocity. The second problem is that temperature or pressure information is needed to know that a discontinuity in the gas density is a shock, and not a contact interface (e.g., the "cold fronts" discussed in § 3.2 below).

X-ray temperature maps of clusters have been used to derive the merger velocities using these relations. Markevitch et al. (1999) used ASCA observations to determine the kinematics of mergers in three clusters (Cygnus-A, Abell 2065, and Abell 3667). Because of the poor angular resolution of ASCA, these analyses were quite uncertain. More recently, possible shocks have been detected in Chandra images of a number of merging clusters (e.g., Abell 85, Kempner et al. 2001; Abell 665, Markevitch et al. 2001; Abell 3667, Vikhlinin et al. 2001b), and the shock jump conditions have been applied to determine the kinematics in these clusters.

The simplest case is a head-on symmetric merger ($b = 0$ and $M_1 = M_2$) at an early stage when the shocked region lies between the two

cluster centers. Markevitch et al. (1999) suggest that the Cygnus-A cluster is an example. If the gas within the shocked region is nearly stationary, then the merger velocity of the two subclusters is just $v = 2\Delta v_s$. Applying these techniques to the ASCA temperature map for the Cygnus-A cluster, Markevitch et al. found a merger velocity of $v \approx 2200$ km/s. This simple argument is in reasonable agreement with the results of numerical simulations of this merger (Ricker & Sarazin 2001). The radial velocity distribution of the galaxies in this cluster is bimodal (Owen et al. 1997), and consistent with a merger velocity of ~2400 km/s.

One can compare the merger velocities derived from the temperature jumps in the merger shocks with the values predicted by free-fall from the turn-around radius (equation 15). In the case of Cygnus-A, Markevitch et al. (1999) found good agreement with the the free-fall velocity of ~2200 km/s. This consistency suggests that the shock energy is effectively thermalized, and that a major fraction does not go into turbulence, magnetic fields, or cosmic rays. Thus, the temperature jumps in merger shocks can provide an important test of the relative roles of thermal and nonthermal processes in clusters of galaxies. Further tests should be possible by comparing shock heating with velocities determined from optical redshifts, from direct velocity measurements in the gas with Astro-E2 and Constellation-X, and from infall arguments.

2.2. NONEQUILIBRIUM EFFECTS

Cluster mergers are expected to produce collisionless shocks, as occurs in supernova remnants. As such, nonequilibrium effects are expected, including nonequipartition of electrons and ions and nonequilibrium ionization (Markevitch et al. 1999; Takizawa 1999,2000). Collisionless shocks are generally not as effective in heating electrons as ions. Assuming that the postshock electrons are somewhat cooler than the ions, the time scale for electron and protons to approach equipartition as a result of Coulomb collisions in a hot ionized gas is (Spitzer 1962)

$$t_{\rm eq} = \frac{3 m_p m_e}{8\sqrt{2\pi} n_e e^4 \ln\Lambda} \left(\frac{kT_e}{m_e}\right)^{3/2} \approx 2.1 \times 10^8 \left(\frac{T_e}{10^8\,{\rm K}}\right)^{3/2} \left(\frac{n_e}{0.001\,{\rm cm^{-3}}}\right)^{-1} {\rm yr}, \qquad (30)$$

where n_e and T_e are the electron number density and temperature, respectively, and Λ is the Coulomb factor. The relative velocity between the postshock gas and the shock front is $(1/4)v_s$; thus, one would expect the electron temperature to reach equipartition at a distance of

$$d_{\rm eq} \approx 160 \left(\frac{v_s}{3000\,{\rm km/s}}\right) \left(\frac{T_e}{10^8\,{\rm K}}\right)^{3/2} \left(\frac{n_e}{0.001\,{\rm cm^{-3}}}\right)^{-1} {\rm kpc} \qquad (31)$$

behind the shock front. Of course, it is the electron temperature (rather than the ion or average temperature) which determines the shape of the X-ray spectrum. This distance is large enough to insure that the lag could be spatially resolved in X-ray observations of low redshift clusters. Similar effects might be expected through non-equilibrium ionization.

On the other hand, it is likely that the nonequilibrium effects in cluster merger shocks are much smaller than those in supernova blast wave shocks because of the low Mach numbers of merger shocks. That is, the preshock gas is already quite hot (both electrons and ions) and highly ionized. Moreover, a significant part of the heating in low Mach number shocks is due to adiabatic compression, and this would still act on the electrons in the postshock gas in merger shocks, even if there were no collisionless heating of electrons. For example, in a $\mathcal{M} = 2$, $\gamma_{\rm ad} = 5/3$ shock, the total shock increase in temperature is a factor of 2.08 (eq. 27). The shock compression is $C = 2.29$, so adiabatic compression increases the electron temperature by a factor of $C^{2/3} = 1.74$, which is about 83% of the shock heating.

3. MERGERS AND COOL CLUSTER CORES

3.1. COOLING FLOWS VS. MERGERS

The centers of a significant fraction of clusters of galaxies have luminous cusps in their X-ray surface brightness known as "cooling flows" (see Fabian 1994 for an extensive review). In every case, there is a bright (cD) galaxy at the center of the cooling flow region. The intracluster gas densities in these regions are much higher than the average values in the outer portions of clusters. X-ray spectra indicate that there are large amounts of gas at low temperatures (down to $\sim 10^7$ K), which are much cooler than those in the outer parts of clusters. The high densities imply rather short cooling times $t_{\rm cool}$ (the time scale for the gas to cool to low temperature due to its own radiation). The hypothesis is that the gas in these regions is cooling from higher intracluster temperature ($\sim 10^8$ K) down to these lower temperatures as a result of the energy loss due to the X-ray emission we observe. Typical cooling rates are $\sim 100\ M_\odot\ {\rm yr}^{-1}$. The cooling times, although much shorter than the Hubble time, are generally much longer than the dynamical time (i.e., sound crossing time) of the gas in these regions. As a result, the gas is believed to remain nearly in hydrostatic equilibrium. Thus, the gas must compress

as it cools to maintain a pressure which can support the weight of the overlying intracluster medium.

The primary observational characteristics of cooling flows are very bright X-ray surface brightnesses which increase rapidly toward the center of the cluster. The high surface brightnesses imply high gas densities which also increase rapidly towards the cluster center. These regions contain cooler cluster gas.

Empirically, there is significant indirect evidence that mergers disrupt cooling flows. There is a strong statistical anticorrelation between cooling flows and/or cooling rates, and irregular structures in clusters as derived by statistical analysis of their X-ray images (Buote & Tsai 1996). The irregular structures are often an indication of an ongoing merger. Looked at individually, very large cooling flows are almost never associated with very irregular or bimodal clusters, which are likely merger candidates (Henriksen 1988; Edge et al. 1992). There are some cases of moderate cooling flows in merging clusters; in most cases, these appear to be early-stage mergers where the merger shocks haven't yet reached the cooling core of the cluster. Examples may include Cygnus-A (Arnaud et al. 1984; Owen et al. 1997; Markevitch et al. 1999) and Abell 85 (Kempner et al. 2001). There also are a large number of merging clusters at a more advanced stage with relatively small cooling cores, both in terms of the cooling rate and the physical radius; Abell 2065 (Markevitch et al. 1999) may be an example. Recently, Chandra Observatory X-ray images have shown a number of merging clusters with rapidly moving cores of cool gas (the "cold fronts" discussed below in § 3.2). In these systems, the cooling flows appear to have survived, at least to the present epoch in the merger.

It is unclear exactly how and under what circumstances mergers disrupt cooling flows. The cooling flows might be disrupted by tidal effects, by shock heating the cooler gas, by removing it dynamically from the center of the cluster due to ram pressure, by mixing it with hotter intracluster gas, or by some other mechanism. Numerical hydrodynamical simulations are needed to study the mechanisms by which cooling flows are disrupted. This is a relatively unexplored area, largely because the small spatial scales and rapid cooling time scales in the inner regions of cooling flows are still a significant challenge to the numerical resolution of hydrodynamical codes. McGlynn & Fabian (1984) argued that mergers disrupted cooling flows, but this was based on purely N-body simulations. Recently, Gómez et al. (2001) have made hydrodynamical simulations of the effects of head-on mergers with relatively small subclusters (1/4 or 1/16 of the mass of the main cluster) on a cooling flow in the main cluster. They find that the mergers disrupt the cooling flow

in some cases, but not in others. Their simulations suggest that the disruption is not due to tidal or other gravitational effects.

Another possibility is that the merger shocks heat up the cooling flow gas and stop the cooling flow. In the simulations, this does not appear to be the main mechanism of cooling flow disruption. There are a number of simple arguments which suggest that merger shocks should be relatively inefficient at disrupting cooling flows. First, it is difficult for these shocks to penetrate the high densities and steep density gradients associated with cooling flows, and the merger shocks would be expected to weaken as they climb these steep density gradients. Even without this weakening, merger shocks have low Mach numbers, and only produce rather modest increases in temperature ($\lesssim$ a factor of 2). These small temperature increases are accompanied by significant compressions. As a result, shock heating actually decreases the cooling time due to thermal bremsstrahlung emission for shocks with Mach numbers $\mathcal{M} \leq (21 + 12\sqrt{3})^{1/2} \approx 6.5$. It is likely that the shocked gas will eventually expand, and adiabatic expansion will lengthen the cooling time. However, even if the gas expands to its preshock pressure, the increase in the cooling time is not very large. For a $\mathcal{M} = 2$ shock, the final cooling time after adiabatic expansion to the original pressure is only about 18% longer than the initial cooling time.

The simulations by Gómez et al. suggest that the main mechanism for disrupting cooling flows is associated with the ram pressure of gas from the merging subcluster. The gas in the cooling flow is displaced, and may eventually mix with the hotter gas (see also Ricker & Sarazin 2001). Earlier, Fabian & Daines (1991) had argued that ram pressure, rather than shock heating, was the main mechanism for disrupting cooling flows. Assuming this is the case, one expects that the merger will remove the cooling flow gas at radii which satisfy

$$\rho_{\rm sc} v_{\rm rel}^2 \gtrsim P_{\rm CF}(r)\,, \tag{32}$$

where $P_{\rm CF}(r)$ is the pressure profile in the cooling flow, $\rho_{\rm sc}$ is the density of the merging subcluster gas at the location of the cooling flow, and $v_{\rm rel}$ is the relative velocity of the merging subcluster gas and the cooling flow. Gómez et al. (2001) find that this relation provides a reasonable approximation to the disruption in their simulations.

The pressure profile in the cooling flow gas prior to the merger is determined by the condition of hydrostatic equilibrium. If the cluster gravitational potential has a wide core within which the potential is nearly constant (e.g., as in a King model), then the cooling flow pressure will not increase rapidly into the center. In this case, once the merger reaches the central regions of the cluster, if the ram pressure is sufficient

to remove the outer parts of the cooling flow, it should be sufficient to remove nearly all of the cooling flow. On the other hand, if the cluster potential is sharply peaked (as in a NFW profile, Navarro et al. 1997), the merger may remove the outer parts of the cooling flow but not the innermost regions. Thus, the survival and size of cool cores in merging clusters can provide evidence on whether clusters have sharply peaked potentials. Markevitch et al. (1999) applied this argument to the two small cool cores in the merging cluster Abell 2065, and concluded that steep central potentials, consistent with the NFW model, were needed.

3.2. COLD FRONTS

One of the more dramatic early discoveries with the Chandra X-ray Observatory was the presence of very sharp surface brightness discontinuities in merging clusters of galaxies. A pair of such discontinuities were first seen in the public science verification data on the Abell 2142 cluster (Markevitch et al. 2000). Initially, it seemed likely that these were merger shocks. However, temperature measurements showed that this was not the case. The high X-ray surface brightness regions were both dense and *cool*, thus, the gas in these regions had a lower specific entropy than the gas in the less dense regions. The lack of a pressure jump and the incorrect sign of the temperature and entropy variations showed that these features could not be shocks (Markevitch et al. 2000). Instead, they appear to be contact discontinuities between hot, diffuse gas and a cloud of colder, denser gas (Markevitch et al. 2000). The cold cloud is moving rapidly through the hotter gas; Vikhlinin et al. (2001b) refer to this situation as a "cold front." Markevitch et al. (2000) argue that the source of the cold clouds are the cooling cores of one or both of merging subclusters. As noted above, cooling flows do appear to be able to partially survive in mergers, at least for some period. Subsequently, cold fronts have been observed in a number of other clusters; for an extensive review of the observations of these cold fronts, see Forman et al. (this volume).

3.2.1 Kinematics of Cold Fronts.

As discussed extensively in Vikhlinin et al. (2001b), the variation in the density, pressure, and temperature of the gas in a cold front can be used to determine the relative velocity of cold core. This technique is analogous to that for merger shocks discussed above (eqs. 28 & 29). The geometry is illustrated in Figure 1.3, which is drawn in the rest frame of the cold core. We assume that the cold core has a smoothly curved, blunt front edge. The normal component of the flow of hot gas past the surface of the cold core will be zero. There will be at least one point where the flow is perpendicular to

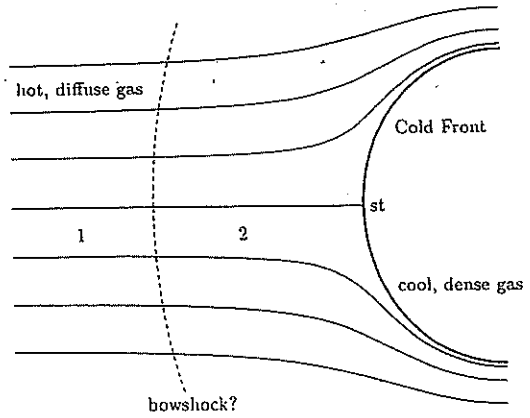

Figure 1.3. A schematic diagram of flow around a "cold front" in a cluster merger. The heavy solid arc at the right represents the contact discontinuity between the cold dense cold core gas, and the hotter, more diffuse gas from the outer regions of the other cluster. The cold core is moving toward the left relative to the hotter gas. The narrow solid lines are streamlines of the flow of the hotter gas around the cold core. The region labelled "1" represent the upstream, undisturbed hot gas. If the cold front is moving transonically ($\mathcal{M}_1 > 1$), then the cold front will be preceded by a bow shock, which is shown as a dashed arc. The stagnation point, where the relative velocity of the cooler dense gas and hotter diffuse gas is zero, is marked "st".

the surface of the cold core, and the flow velocity of the hot gas will be zero at this stagnation point ("st" in Fig. 1.3). Far upstream, the flow of the hot gas will be undisturbed at the velocity of the cold core relative to the hotter gas, v_1. Let c_{s1} be the sound speed in this upstream gas and $\mathcal{M}_1 \equiv v_1/c_{s1}$ be the Mach number of the motion of the cold core into the upstream gas. If $\mathcal{M}_1 > 1$, a bow shock will be located ahead of the cold front.

The ratio of the pressure at the stagnation point to that far upstream is given by (e.g., Landau & Lifshitz 1959, § 114).

$$\frac{P_{\rm st}}{P_1} = \begin{cases} \left(1 + \frac{\gamma_{\rm ad}-1}{2}\mathcal{M}_1^2\right)^{\frac{\gamma_{\rm ad}}{\gamma_{\rm ad}-1}}, & \mathcal{M}_1 \le 1, \\ \mathcal{M}_1^2 \left(\frac{\gamma_{\rm ad}+1}{2}\right)^{\frac{\gamma_{\rm ad}+1}{\gamma_{\rm ad}-1}} \left(\gamma_{\rm ad} - \frac{\gamma_{\rm ad}-1}{2\mathcal{M}_1^2}\right)^{-\frac{1}{\gamma_{\rm ad}-1}}, & \mathcal{M}_1 > 1. \end{cases} \quad (33$$

The ratio $(P_{\rm st}/P_1)$ increases continuously and monotonically with $\mathcal{M}_1$. Thus, in principle, measurements of P_1 and $P_{\rm st}$ in the hot gas could be used to determine $\mathcal{M}_1$. The pressures would be determined from X-ray spectra and images. In practice, the emissivity of the hot gas near the stagnation point is likely to be small. However, the pressure is continuous across the cold front, so the stagnation pressure can be determined just inside of the cold core, where the X-ray emissivity i

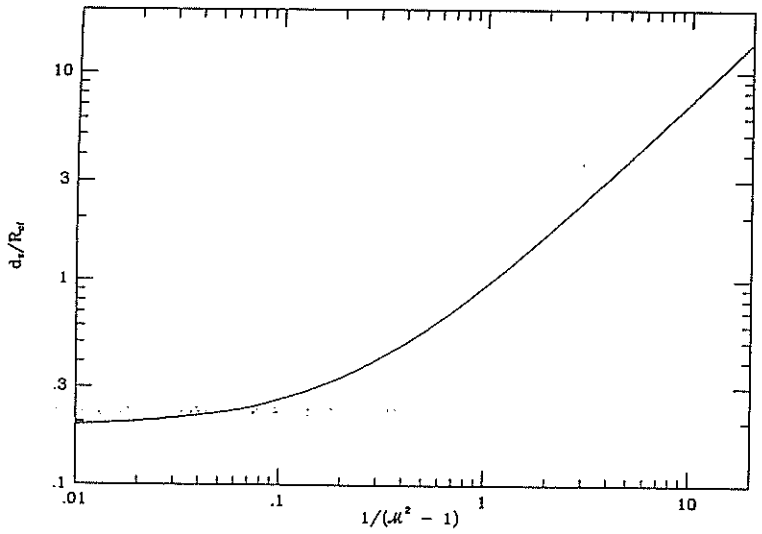

Figure 1.4. The ratio of the stand-off distance of the bow shock d_s to the radius of curvature $R_{\rm cf}$ of the stagnation region of the cold front, as a function of $1/(\mathcal{M}_1^2 - 1)$, where $\mathcal{M}_1$ is the Mach number. This is for a spherical cold front and $\gamma_{\rm ad} = 5/3$.

likely to be much higher. Once $\mathcal{M}_1$ has been determined, the velocity of the encounter is given by $v_1 = \mathcal{M}_1 c_{s1}$.

If the motion of the cold core is transonic ($\mathcal{M}_1 > 1$), one can also determine the velocity from the temperature and/or density jump at the bow shock (eqs. 28 & 29). If the bow shock can be traced to a large transverse distance and forms a cone, the opening angle of this Mach cone corresponds to the Mach angle, $\theta_M \equiv \csc^{-1}(\mathcal{M}_1)$. However, variations in the cluster gas temperature may lead to distortions in this shape.

The distance between the stagnation point and the closest point on the bow shock (the shock "stand-off" distance d_s) can also be used to estimate the Mach number of the motion of the cold front (Vikhlinin et al. 2001b). The ratio of d_s to the radius of curvature of the cold front $R_{\rm cf}$ depends on the Mach number $\mathcal{M}_1$ and on the shape of the cold front. Figure 1.4 shows the values of $d_s/R_{\rm cf}$ as a function of $(\mathcal{M}_1^2 - 1)^{-1}$ for a spherical cold front (Schreier 1982).

Although there is no simple analytic expression for the stand-off distance which applies to all shapes of objects, a fairly general approximate method to calculate d_s has been given by Moekel (1949), and some simple approximate expressions exist for a number of simple geometries (Guy 1974; Radvogin 1974). The stand-off distance increases as the Mach number approaches unity; thus, this method is, in some ways, a very sensitive diagnostic for the Mach number for the low values expected in cluster mergers. On the other hand, the stand-off distance also depends strongly on the shape of the cold front as the Mach number decreases. The application of this diagnostic to observed clusters is strongly affected by projection effects. Because the radius of curvature of the bow shock is usually greater than that of the cold front (Rusanov 1976), projection effects will generally cause d_s to be overestimated and $\mathcal{M}_1$ to be underestimated. Projection effects also make the true shape of the cold front uncertain.

These techniques have been used to determine the merger velocities from cold fronts in Abell 3667 (Vikhlinin et al. 2001b), RX J1720.1+2638 (Mazzotta et al. 2001), and Abell 85 (Kempner et al. 2001).

3.2.2 Width of Cold Fronts.

One remarkable aspect of the cold fronts observed with the Chandra Observatory in several clusters is their sharpness. In Abell 3667, the temperature changes by about a factor of two across the cold front (Vikhlinin et al. 2001b), and the accompanying change in the X-ray surface brightness occurs in a region which is narrower than 2 kpc (Vikhlinin et al. 2001b). This is less than the mean-free-path of electrons in this region. The existence of this very steep temperature gradient and similar results in other merging clusters with cold fronts requires that thermal conduction be suppressed by a large factor (Ettori & Fabian 2000; Vikhlinin et al. 2001a,b) relative to the classical value in an unmagnetized plasma (e.g., Spitzer 1962). It is likely that this suppression is due to the effects of the intracluster magnetic field. It is uncertain at this point whether this is due to a generally tangled magnetic field (in which case, heat conduction might be suppressed throughout clusters), or due to a tangential magnetic field specific to the tangential flow at the cold front (Vikhlinin et al. 2001a).

Because of the tangential shear flow at the cold front (Fig. 1.3), the front should be disturbed and broadened by the Kelvin-Helmholtz (K-H) instability. Vikhlinin et al. (2001a) argue that the instability is suppressed by a tangential magnetic field, which is itself generated by the tangential flow. This suppression requires that the magnetic pressure P_B be a non-trivial fraction of the gas pressure P in this regions, $P_B \gtrsim 0.1P$. The required magnetic field strength in Abell 3667 is $B \sim 10\ \mu$G.

4. NONTHERMAL PHYSICS OF MERGER SHOCKS

Cluster mergers involve shocks with velocities of ~2000 km/s. Radio observations of supernova remnants indicate that shocks with these ve-

Saraswat 2002 da eq. 17 ad eq 18

$$J_1 = \frac{\lambda G}{a^{1/2}} M_1^{5/3} \qquad J_2 = \frac{\lambda G}{a^{1/2}} M_2^{5/3}$$

$$J_{TOT} = J_1 + J_2 + J_{orb}$$

$$J_{orb} = J_{TOT} - J_1 - J_2 = \frac{\lambda G}{a^{1/2}} \left[(M_1+M_2)^{5/3} - M_1^{5/3} - M_2^{5/3} \right] =$$

$$= \frac{\lambda G}{a^{1/2}} (M_1+M_2)^{5/3} \left[1 - \frac{M_1^{5/3} + M_2^{5/3}}{(M_1+M_2)^{5/3}} \right]$$

$$E_1 = a M_1^{5/3} \qquad E_2 = a M_2^{5/3}$$

$$E_{TOT} = E_1 + E_2 + E_{orb}$$

$$E_{orb} = E_{TOT} - E_1 - E_2 = \underbrace{\frac{G M_1 M_2}{d_0} - \frac{1}{2} \frac{M_1 M_2}{M_1+M_2} v_0^2}_{\text{eq. 14}} = a \left[(M_1+M_2)^{5/3} - M_1^{5/3} - M_2^{5/3} \right]$$

$$a = \frac{\left(\frac{G M_1 M_2}{d_0} - \frac{1}{2} \frac{M_1 M_2}{M_1+M_2} v_0^2 \right)}{(M_1+M_2)^{5/3} \left[1 - \frac{M_1^{5/3} + M_2^{5/3}}{(M_1+M_2)^{5/3}} \right]}$$

$$J_{orb} = \frac{\lambda G \, (M_1+M_2)^{5/3+5/6}}{\left(\frac{G(M_1+M_2)}{d_0} - \frac{1}{2} v_0^2 \right)^{1/2} \cdot \left(\frac{M_1 M_2}{M_1+M_2} \right)^{1/2}} \left[1 - \frac{M_1^{5/3} + M_2^{5/3}}{(M_1+M_2)^{5/3}} \right]^{1+\frac{1}{2}} =$$

$$= \frac{\lambda G \, M_1 M_2}{(\quad)^{1/2}} \cdot \underbrace{\frac{(M_1+M_2)^{3/2}}{M_1^{3/2} M_2^{3/2}} \left[\quad \right]^{3/2}}_{f(M_1, M_2)}$$

eq. 18 e 19

TABLE 5

MASS AND LUMINOSITY CALCULATIONS

A. A2197

Subsample	R_s ($\times 10^{24}$ cm)	M_t ($\times 10^{15}\ M_\odot$)	L_t ($\times 10^{15}\ L_\odot$)	M/L (solar units)
$r < 0.4$	1.26	21.2	1.0	212
$r < 0.6$	1.59	5.5	2.2	25
$r < 0.876$.....	2.26	2.5	3.2	8

B. A2199

Subsample	R_s ($\times 10^{24}$ cm)	M_t ($\times 10^{15}\ M_\odot$)	L_t ($\times 10^{15}\ L_\odot$)	M/L (solar units)
$r < 0.4$	1.09	19.2	0.6	320
$r < 0.6$	1.66	25.6	1.5	171
$r < 0.852$.....	2.24	13.2	2.2	60

Zwicky magnitudes in any other locale to provide an approximate total luminosity for that locale which is then scaled up to the $m_p = 17.5$ limit of the BGP sample.

We must also include some correction for internal absorption within the individual galaxies. To do so, we follow the results outlined by Thompson, Welker, and Gregory (1978), who determined an average correction for a sample of galaxies with an E:S0:S+Ir distribution of 10%:28%:62%. This correction amounts to -0.35 mag, which we apply to all samples but those in the central cluster cores ($r < 0.^\circ 4$). Finally, we must adopt a distance to determine the cluster distance modulus. For this purpose we adopt $d = 91.66/h$ Mpc, and we find a distance modulus of $m - M = 34.81 - 5 \log h$.

Using all corrections given above, we calculate the luminosities and M/L ratios shown in columns (4) and (5) of Table 5. Part A of this table gives the results for A2197, and part B for A2199. The outer samples indicate a decrease of M/L as a function of distance from the cluster core.

d) Double Cluster Infall Analysis

The binary nature of the A2197/A2199 system provides a nearly unique opportunity of determining cluster masses independent of the virial technique. The analysis described here was originally outlined by Thompson (1982) and it starts with the formalism introduced by Peebles (1971) and Gunn (1974). The unique character of the following solution lies in the fact that the total system mass and M/L ratio are determined as a function of the projection angle α between the plane of the sky and the line connecting the cluster centers (i.e., $\alpha = 0$ if the two clusters are at precisely the same cosmological distances from the observer). Consequently we find a set of solutions which depend on α.

Let us clearly state that the solution rests on the simplifying assumptions of a simple two-body problem with linear motion (i.e., no rotational support) and boundary values of $R = 0$ at $T = 0$. We start with the well-known parameterized solutions to the field equations, with separate solutions for the bound and unbound cases:

Bound	Unbound	
$R = \frac{R_m}{2}(1 - \cos\chi)$	$R = \frac{GM}{v_\infty^2}(\cosh\chi - 1)$	(1)
$T = \left(\frac{R_m^3}{8GM}\right)^{1/2}(\chi - \sin\chi)$	$T = \frac{GM}{v_\infty^3}(\sinh\chi - \chi)$	(2)
$V = \left(\frac{2GM}{R_m}\right)^{1/2}\frac{\sin\chi}{1 - \cos\chi}$	$V = V_\infty\frac{\sinh\chi}{\cosh\chi - 1}$.	(3)

The relationship between R_p (the projected separation on the plane of the sky) and R (the true spatial separation) is the simple geometrical equality

$$R_p = R\cos\alpha, \tag{4}$$

where $R_p = 6.25/h \times 10^{24}$ cm; and similarly the true relative velocity V and the observed radial velocity V_R are related by

$$V_R = V\sin\alpha, \tag{5}$$

where $V_R = 194 \pm 77$ km s^{-1}.

After substituting equations (4) and (5) into equations (1)–(3), it becomes obvious that the problem is overdetermined, and that a

Metodo osservativi X × metto intracluster (ICM)

DA BRILLANTA SUPERFICIALE

RISULTATI MOLTO BUONI ($R_{500} \sim \frac{R_{vir}}{2}$)
× CENTRAL REGIONS
CATTIVI × R GRANDI

2D contorni di ~~isodensità~~

iso - brillanza superficiale (~ iso-densità del gas)

$\epsilon_\nu \propto \rho_{gas}^2 \cdot T_x^{1/2}$

classificazione morfologica di Jones e Forman 82

• center shift di Mohr

2D + quantitativo • metodo dei "power ratio" di Buote

Momenti del potenziale gravitazionale (2D) "pseudopotenziale"

calcolato entro un raggio R

$m=0$ $P_0 = [a_0 \ln(R)]^2$ con origine sul Centro di massa oppure sul picco X

$m>0$ $P_m = \frac{1}{2m^2 R^{2m}} (a_m^2 + b_m^2)$

$$a_m(R) = \int_{R' \le R} \Sigma(\bar{x}')(R')^m \cos(m\phi') d^2\bar{x}'$$

$$b_m(R) = \int_{R' \le R} \Sigma(\bar{x}')(R')^m \sin(m\phi) d^2\bar{x}'$$

dove $\bar{x}' = (R', \phi')$ → angolo azimutale

$\frac{P_1}{P_0}$ ~ center shift $\frac{P_2}{P_0}$ ~ ellitticità $\frac{P_3}{P_0}$ ~ sottostrutture

Evoluzione nel piano $P_2/P_0 - P_3/P_0$

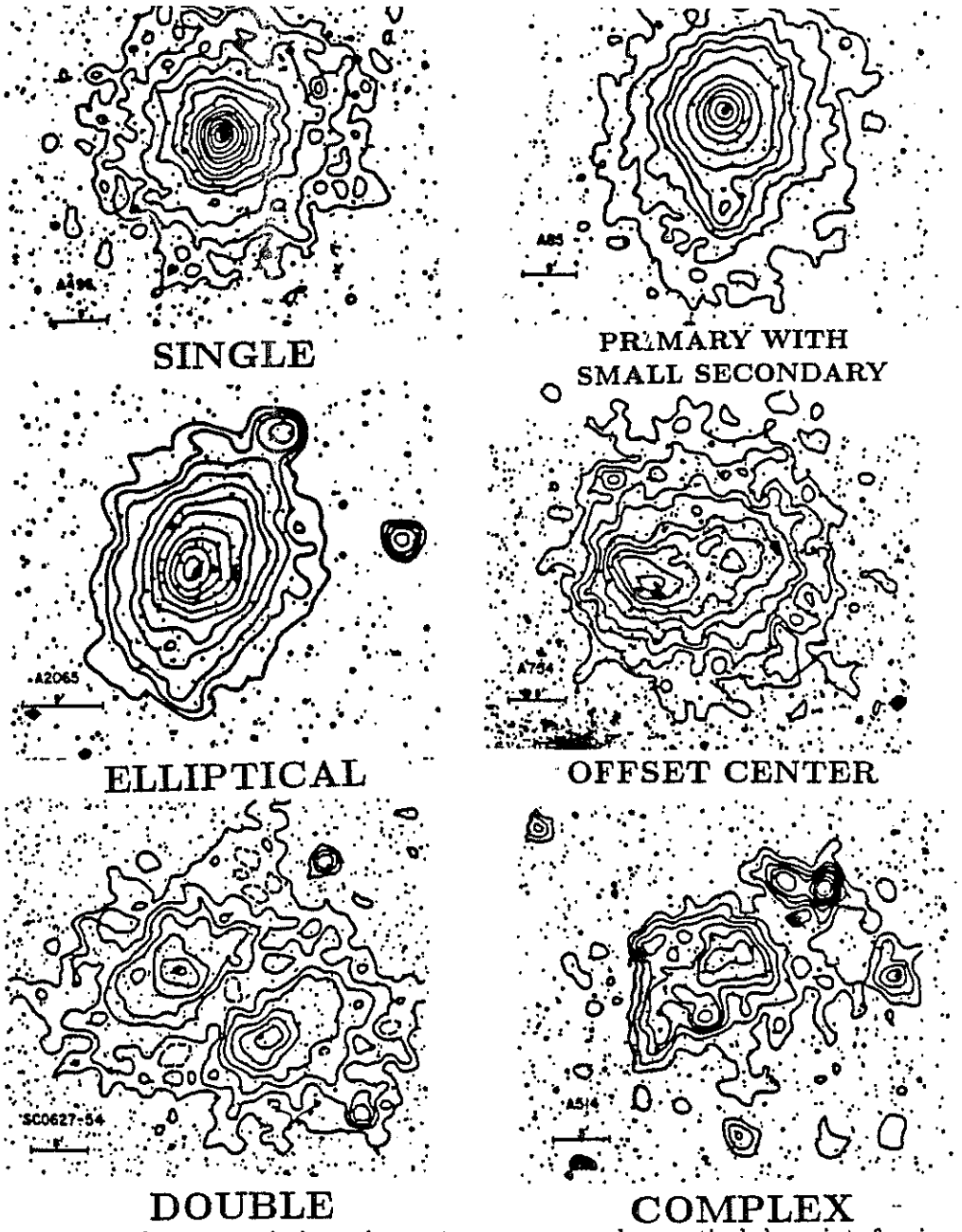

Figure 11 shows x-ray isointensity contours superposed on optical sky prints for six x-ray defined cluster morphological classes.

Jones e Forman 82

(vedi anche Sarazin 86)

cation according to dynamical states, we have not distinguished [illegible] between the different classes of highly disturbed clusters (i.e., complex and double). Since there is nothing special about the 1 Mpc aperture it is sensible to explore the effects of using different apertures. The result of computing the power ratios in a 0.5 Mpc aperture is displayed in Figure 3.7

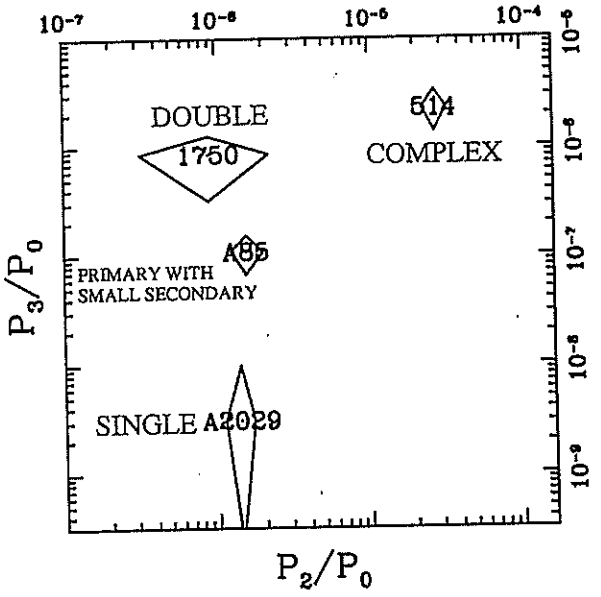

Figure 3.7. As Figure 3.6 but for the 0.5 Mpc aperture.

By focusing initially on P_2/P_0 it can be seen that three of the clusters appear to be relaxed systems (i.e., small P_2/P_0). This is because the 0.5 Mpc aperture only encloses 1 component of the double cluster and only the primary component of A85. The single component cluster A2029 appears relaxed on both the 0.5 and 1 Mpc scales. However, A514 is complex on many scales and it is easily distinguished from the other reference clusters as a disturbed system in the 0.5 Mpc aperture. Of course, one only needs to appeal to P_3/P_0 to verify that both the double and complex clusters are actually in a younger dynamical state than the others. Hence, the power ratios represent a quantitative implementation of the Jones & Forman classification scheme, particularly on the 0.5 Mpc scale.

2.2. MERGER FREQUENCY OF ROSAT CLUSTERS

The result of computing power ratios for the brightest ~ 40 *ROSAT* clusters is displayed in Figure 3.8. It is immediately apparent that there is a marked deficiency of highly disturbed clusters (complex and double). These brightest clusters therefore lack young members and are instead dominated by mostly evolved clusters with only small-scale (< 500 kpc) substructure. Since such highly evolved clusters are usually associated with cooling flows it should be expected that cooling flows dominate the brightest clusters as has been suggested before on different grounds (e.g., Arnaud 1988; Forman & Jones 1990; Edge et al. 1992; Peres et al. 1998).

In Figure 3.9 the quantitative connection between cooling flows and cluster morphology is shown by the anti-correlation of the mass deposition rate ($\dot{M}$) and P_2/P_0. This represents the first quantitative description of the anti-correlation of substructure with the strength of a cooling flow. Note the large scatter for systems that have significant substructure (i.e., large P_2/P_0). Analysis of this correlation and its large scatter should shed light on how cooling flows are disrupted by mergers and are subsequently re-established.

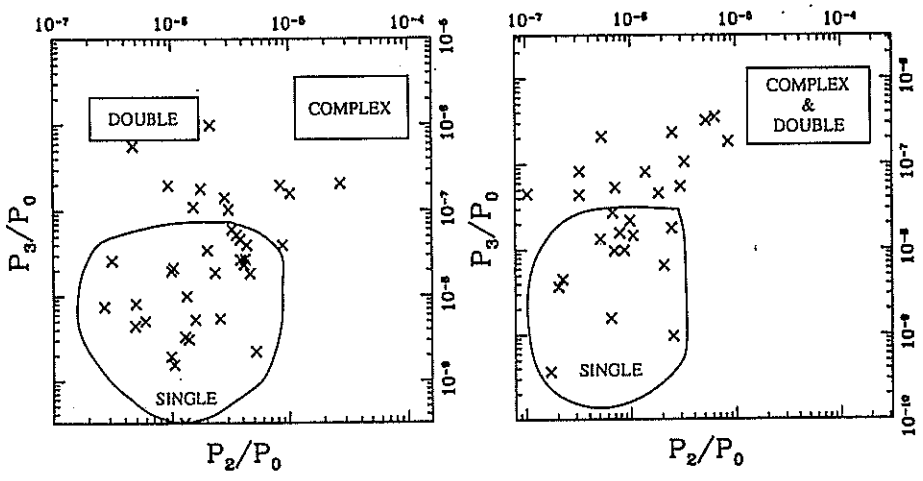

Figure 3.8. Power ratios of the brightest ~ 40 clusters (Buote & Tsai 1996) computed within apertures of 0.5 Mpc (Left) and 1 Mpc (Right).

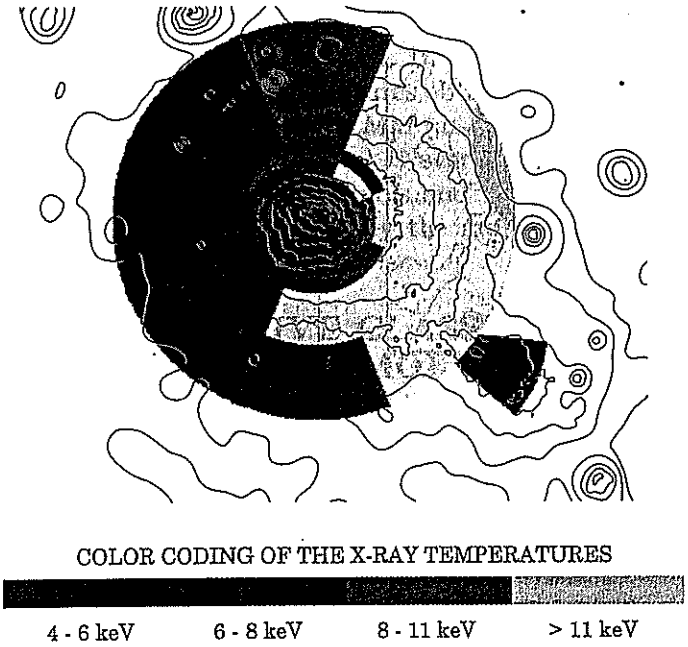

Figure 3.15. *ROSAT* temperature map of the Coma cluster (Briel & Henry 1998).

with any precision for all but a small number of the brightest clusters. For these clusters the S/N was so high that the data from the spectra below 2 keV managed to place interesting constraints on the temperature.

For example, the *ROSAT* temperature map of Coma (Briel & Henry 1998) displayed in Figure 3.15 shows significant temperature variations. The region of hotter gas in between the main cluster and the NGC 4839 subcluster is consistent with shock heating during the passage of the subcluster through the main cluster (e.g., Burns et al. 1994; Ishizaka & Mineshige 1996). However, further simulations are required to establish whether the subcluster is currently falling in or has already passed through the main cluster. As noted by Briel & Henry (1998) if the subcluster already passed though the main body then it is unclear why the subcluster still has retained its halo of hot gas. Other *ROSAT* temperature maps of mergers display similar evidence for shock-heating (e.g., Briel & Henry 1994; Henry & Briel 1995, 1996; Ettori et al. 2000).

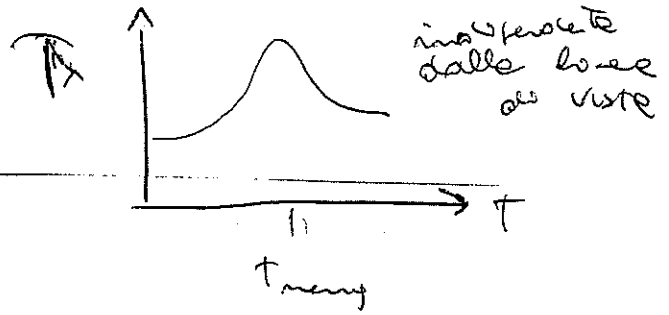

β spettrale ~ 1
anche in sottostrutture

obtained from *ASCA* data depending on the PSF deconvolution procedure used (see White 2000; Irwin & Bregman 2000 and references therein) the detailed temperature features obtained with *ASCA* do need to be confirmed with *Chandra* and *XMM* (as do those with *BeppoSAX* because of its low spatial resolution.) Nevertheless, the overall trend of non-azimuthal temperature structures and the shock-heating of the intra-cluster medium are supported by the available *ROSAT*, *ASCA*, and *BeppoSAX* data.

6.2. QUANTITATIVE CLASSIFICATION OF TEMPERATURE MORPHOLOGY

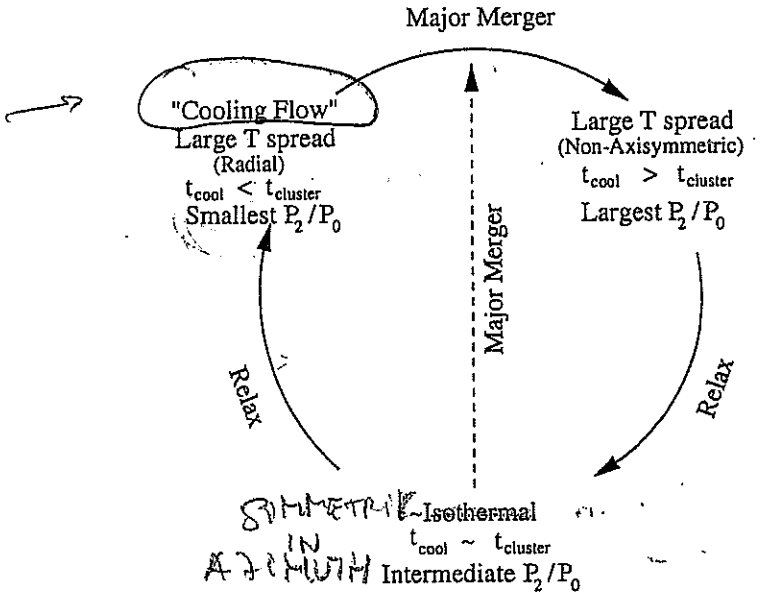

Figure 3.17. A possible description of the evolution of the X-ray temperature structure and image morphology during the formation and evolution of a cluster.

To obtain a more complete picture of the current dynamical states and the merger histories of clusters the global morphological classification of cluster images discussed in § 2 should also incorporate the morphologies of X-ray temperature maps. In Figure 3.17 I show an idealized picture of how the temperature morphology of a cluster might evolve during a merger. At early times there is a large spread of temperatures dis-

Metodo osservazioni dell'X (ct.)

Presenza del "cooling flow"
ora "cool core" è legata
al rilassamento dinamico:
merger distrugge i cool core!
che poi si può riformare.

Da innalzamento T_X (visto anche da simulazioni $T_{oss} > T_{virale}$, ma è indipendente da α, angolo di proiezione)

Zone a T alta e zone a T basse.
MAPPE DI TEMPERATURE
shock etc,

CLUSTER MERGER / RADIO HALOS

(Merging processes in galaxy clusters – Feretti, Gioia, Giovannini 2002
– Sarazin – Girardi e Biviano – Giovannini e Feretti)

OBSERVATIONAL PHENOMENOLOGY

cluster substructures 30–50% Frequency (small) 10% $M_{cluster}$
(bimodal)

↑

cluster mergers

extese radio emission (300, 800 MHz, 1.6 GHz e.g. 21 cm 1420 MHz)

SIZE ~1 Mpc

Halo	relic
(central)	(elongated, peripheric)
	1959 COMA C
	1970 Wilson
	Hanish 1982

SPECTRUM

steep radio spectrum $I \propto \nu^{-\alpha}$ $\alpha \sim 1.2$ ⟹ SYNCHROTRON EMISSION by non-thermal relativistic electron in a magnetic field ($\lesssim 1\,\mu G$)

(relic highly polarized)

FREQUENCY

10% of clusters

33% in clusters with high L_X

PROPERTIES

$P_R - T_X$ relation

Size $- T_X$

ORIGIN

e⁻ population OK

1) origin from strong radio sources
2) accelerated out of the thermal pools
3) shocks from earlier mergers

elect.

$\gamma = 300$ Lorentz factor

$E = \gamma m_e c^2 \sim 150$ MeV → $t_{life} = 10^9$ y

$\gamma \sim 10^4 \rightarrow t = 10^8$ y

magnetic field OK

rotation measure OK

ORIGIN OF RADIO HALOS (Ct.)

The difficulty in explaining radio halos arises from the combination of their large size (1 Mpc = $3 \cdot 10^{6}$-10^{8} km = $= 3 \cdot 10^{19}$ Km ; 1 y = $3 \cdot 10^{7}$ s) and the short synchrotron lifetime (10^{8} y) of relativistic electrons.
The expected diffusion velocity of the electron population is of the order of the Alfven speed (~ 100 Km/s) making it difficult for electrons to diffuse over a scale region within their radiative lifetime ($S = v \cdot t \leq$ Mpc)

- PRIMARY ELECTRON MODELS — NO! on Mpc scale
- PRIMARY ELECTRON REACCELERATION MODELS
continuous in-situ reacceleration of the radiating electrons by turbulent magnetic field
cluster mergers (shocks and Turbulence)
radio halo

(Tribble 93) SPIEGA TUTTO:
energetics involved in a merger are more than enough to power a radio halo releasing gravitational binding energies ~ 10^{64} erg
then by hidrodyn. shocks dissipate energy of $3 \cdot 10^{63}$ erg
$\Delta V \sim 1000$-2000 Km/s
$M \sim 10^{14} M_{\odot}$ ↳ 10^{33} g

frequency 10^{8} y radiative lifetime / Time interval between major mergers ~ 10^{9} y ⟸ radio halos are Transient (= rare) phenomena
associations between radio halos and mergers

- SECONDARY ELECTRON REACCELERATION MODELS
radio emission results from a population of secondary electrons resulting from inelastic collisions between relativistic p^{+} and the thermal ions of ICM, p^{+} diffuse on large scales (their energy losses are negligible) and produce e^{-} in situ

THE ASTROPHYSICAL JOURNAL, 567:L27–L31, 2002 March 1

A TEXTBOOK EXAMPLE OF A BOW SHOCK IN THE MERGING GALAXY CLUSTER 1E 0657−56

M. MARKEVITCH, A. H. GONZALEZ, L. DAVID, A. VIKHLININ, S. MURRAY, W. FORMAN, C. JONES, AND W. TUCKER[1]
Harvard-Smithsonian Center for Astrophysics, 60 Garden Street, Cambridge, MA 02138; maxim@head-cfa.harvard.edu
Received 2001 October 21; accepted 2002 January 15; published 2002 February 12

ABSTRACT

The *Chandra* image of the merging, hot galaxy cluster 1E 0657−56 reveals a bow shock propagating in front of a bullet-like gas cloud just exiting the disrupted cluster core. This is the first clear example of a shock front in a cluster. From the jumps in the gas density and temperature at the shock, the Mach number of the bullet-like cloud is 2–3. This corresponds to a velocity of 3000–4000 km s^{-1} relative to the main cluster, which means that the cloud traversed the core just 0.1–0.2 Gyr ago. The 6–7 keV "bullet" appears to be a remnant of a dense cooling flow region once located at the center of a merging subcluster whose outer gas has been stripped by ram pressure. The bullet's shape indicates that it is near the final stage of being destroyed by ram pressure and gasdynamic instabilities, as the subcluster galaxies move well ahead of the cool gas. The unique simplicity of the shock front and bullet geometry in 1E 0657−56 may allow a number of interesting future measurements. The cluster's average temperature is 14–15 keV but shows large spatial variations. The hottest gas ($T > 20$ keV) lies in the region of the radio halo enhancement and extensive merging activity involving subclusters other than the bullet.

Subject headings: galaxies: clusters: individual (1E 0657−56) — intergalactic medium — X-rays: galaxies

1. INTRODUCTION

Galaxy clusters form via mergers of smaller subunits. Such mergers dissipate a large fraction of the subclusters' vast kinetic energy through gasdynamic shocks, heating the intracluster gas and probably accelerating high-energy particles (e.g., Sarazin 2001 and references therein). Shocks contain information on the velocity and geometry of the merger. They also provide a unique laboratory for studying the intracluster plasma, including such processes as thermal conduction and electron-ion equilibration (e.g., Shafranov 1957; Takizawa 1999). Some exploratory uses of X-ray data on cluster shocks were described by Markevitch, Sarazin, & Vikhlinin (1999). While many merging clusters exhibit recently heated gas (see, e.g., Henry & Briel 1995, Markevitch et al. 1999, Furusho et al. 2001, and references in those works; Neumann et al. 2001), so far only two candidate merger shock fronts were observed. One is a mild X-ray brightness edge, apparently a shock with a Mach number near 1, preceding the prominent "cold front" in A3667 (Vikhlinin, Markevitch, & Murray 2001). Another is a hot region in front of the A665 core (Markevitch & Vikhlinin 2001, hereafter MV) that shows no clear density jump, perhaps because of an unfavorable viewing geometry.

The *Chandra* observation of 1E 0657−56 presents the first clear example of a cluster bow shock. This $z = 0.296$ cluster was discovered by Tucker, Tananbaum, & Remillard (1995) as an *Einstein* IPC extended source. From *ASCA* data, Tucker et al. (1998, hereafter T98) derived a temperature around 17 keV, making this system one of the hottest known (see also Yaqoob 1999 and Liang et al. 2000, hereafter LHBA). *ROSAT* data show that 1E 0657−56 is a merger (T98). It also hosts the most luminous synchrotron radio halo (LHBA).

Below we present results from the *Chandra* observation of 1E 0657−56 performed in 2000 October. We use $H_0 = 100\ h$ km s^{-1} Mpc^{-1} and $\Omega_0 = 0.3$, $\Lambda = 0$; $1' = 0.172\ h^{-1}$ Mpc at the cluster redshift. Confidence intervals are 90% for one parameter, unless specified otherwise.

[1] Also at the University of California, San Diego.

2. DATA ANALYSIS

1E 0657−56 was observed by ACIS-I at the focal-plane temperature of −120°C for a useful exposure of 24.3 ks. To derive the gas temperature for a given region of the cluster image, the telescope and detector response were modeled as described in MV. The ACIS background rate did not vary during the exposure but was higher than expected by a factor of about 1.3, most likely due to anomalous "space weather." This required special background modeling. To do this, we extracted a spectrum from the ACIS-I region outside an $r = 8'.6$ (1.5 h^{-1} Mpc) circle centered on the cluster, which should be free of cluster emission. Point sources were excluded. The observed excess over the nominal background[2] was well modeled in the 0.7–10 keV band by the sum of two power laws E^{α} with photon indices $\alpha = -0.6$ and 3.0 (dominant below and above $E \sim 5$ keV, respectively) originating inside the detector, i.e., without applying the mirror effective area and CCD efficiency to the model. Such a background anomaly in the ACIS-I chips is rare and not yet understood. We assumed that this component is distributed uniformly over the detector and added it (normalized by solid angle) to the nominal background spectra. High-energy residuals in the overall cluster fit indicated that the normalization of the corrected background required an additional 10% increase (perhaps indicating some spatial nonuniformity of the excess), which we applied to the spectra from all cluster regions.

To make a 0.5–5 keV image for the gas density analysis, we compared the observed background rate far from the cluster with the nominal model background (without the above additional component) and derived a correction factor of 1.35 for this wide band, which was applied to the model background image. This is of course consistent with the above spectral correction. A 10% background uncertainty was included in deriving the confidence intervals for all quantities. This approximate background modeling is adequate for our present

[2] A combination of blank-field observations normalized by the exposure time (see http://asc.harvard.edu/cal, click "ACIS," then "ACIS Background").

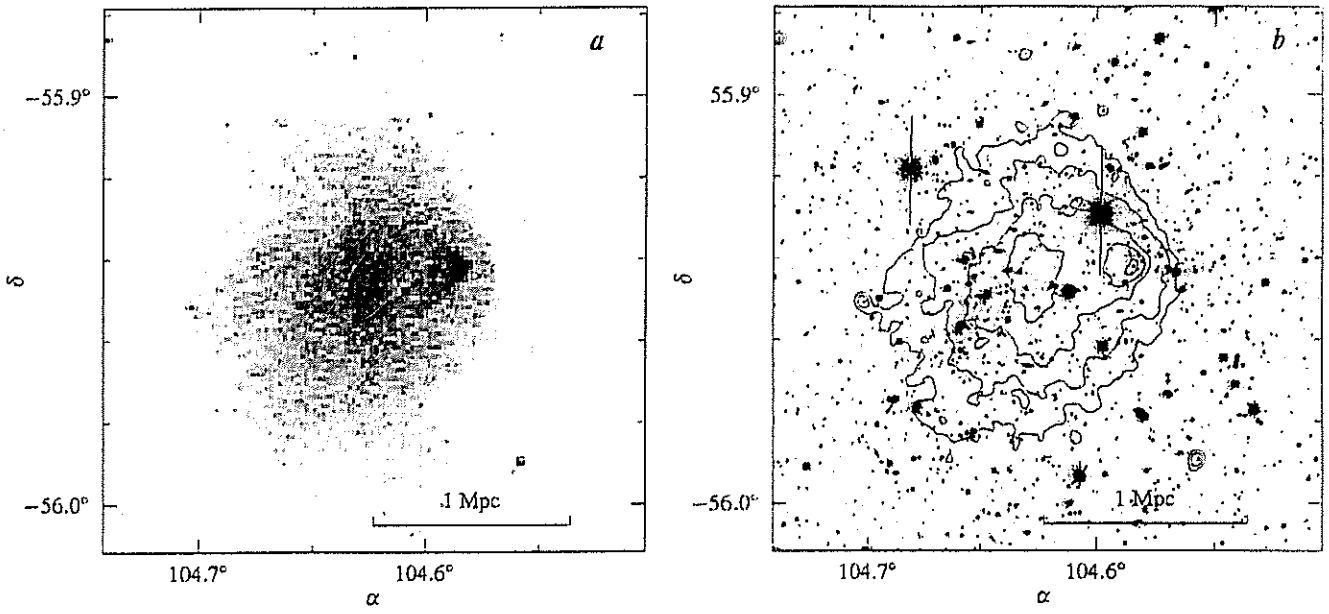
a
b
−55.9°
−56.0°
55.9°
δ
104.7°
104.6°
α
1 Mpc

BRADAC et al 2006